Authors response - AMT

Application of the shipborne remote sensing supersite OCEANET for profiling of Arctic aerosols and clouds during Polarstern cruise PS106 – Griesche et al.

Response to Anonymous Referee #1 (16 January 2020)

We would like to thank the Anonymous Referee #1 for spending time in order to provide us with fruitful comments and suggestions and thus to help us to improve the manuscript. The initial submission has been adapted, and we hope that the manuscript is now acceptable for publication.

Our point-by-point response to the review comments is written here in bold font. The marked-up manuscript version with all changes compared to the initial submission is attached to this file and its line numbering is used to reference changes below.

Overall summary of major changes:

We would like to inform the referee about the following major changes:

- **Revision of the abstract due to suggestion of Referee #2**
- **Reprocessing of the Cloudnet data with an Arctic MWR-retrieval considering the comments of both Referee #1 and #2**
- **Included a better evaluation of the capabilities of the motion stabilization according to comments by both Referee #1 and #2**
- **Improved the discussion of the eddy dissipation rate and fog/low-stratus retrievals as well as Cloudnet in general considering the comments by both Referee #1 and #2**

Detailed responses:

This paper presents the instruments deployed on the icebreaker Polarstern and close by on a temporary ice-camp and results obtained during a summer cruise performed in the frame of the AC3 German project in 2017. Several remote sensing equipment, including a motion-stabilized 35-GHz cloud radar were deployed and combined with meteorological observations in high Arctic. This experiment concurred to a very important goal on a better documentation and understanding of Arctic change, through the presentation of a campaign and results obtained to better document Arctic cloud forcing. After introducing the context, this paper first gives a general description of the instrumentation deployed on board the ice-breaker Polarstern and on the ice camp, technical challenges, new developments, analysis methods and results obtained during the campaign. It finally focuses on case studies.
Two main points are highlighted in the paper which are 1) the first involvement of the cloud radar Mira-35 and the development of a motion stabilization system to ensure stable observations. Corrections and results obtained from vertical wind spectra to derive on the turbulent kinetic energy eddy dissipation rate (EDR) are presented; 2) the focus on low-level clouds and the

presence of fog from synergies of lidar and radar within Cloudnet, and the retrieval of radiative cloud properties.

The topic is of importance to the community. The paper is clearly written, and presented in a very comprehensive way. The context of the paper is well introduced although additional general information should be given on existing surface based observations. The two main points presented also need some additional information and discussion. The paper is worth publishing after minor revisions are made. They are addressed here below.

Detailed comments Page 2, line 27 : “decline of the Arctic sea ice” precision to be added on period of the year (summer ?) or ice type (multi-year sea-ice) ?
We added details “This is observed as a change of several parameters such as the drastic decline of the Arctic sea ice during all seasons, but especially in summer, in both extend and thickness”. See line 33.

Page 2, line 45-47 : Arctic observations refer to aircraft and shipborne measurements, but Arctic ground-based stations should be discussed (IASOA network, Uttal et aL, BAMS 2016 DOI:10.1175/BAMS-D-14-00145.1) in which remote sensing instruments are implemented at Barrow (Dong et al., 2010, doi:10.1029/2009JD013489, Eureka (Blanchard et al., JAMC 2014 doi: 10.1175/JAMC-D-14-0021.1) for example. Drifting buoys have also recently been equipped in the high Arctic with lidar in the frame of the IAOOS project (DiBiagio et al., JGR 2018, doi: 10.1002/2017JD027530 ; Mariage et al., Opt. Exp. 2016, doi: 10.1364/OE.25.000A73).
We extended the discussion about ground-based stations and buoy observations, as requested. See lines: 51-57.

Page 2, line 54, replace by a more recent reference Winker et al., BAMS, 2010, doi:10.1175/2010BAMS3009.1.
Done

Page 4, line 88 : Figure 1 legend : mark days also on the track in the upper figure
We added some dates for orientation also into the top subfigure of Fig. 1.

Page 4, line 94 : mention if Polar measurements have already been performed ?
We added information about previous cruises to lines 111-112.

Page 5, lines 103 and 104 : 532 instead of 512 ?
Corrected

Page 5, line 110: “allow to determine the shape” this is too strong a statement. As the authors write further in the text, it allows to discriminate shape between spherical and non-spherical particles, but several shapes can give the same depolarization ratio
We rephrased the respective passage in the text and provide references to the available applications of polarization measurements. See lines 129-130.

Page 6, lines 125-26 : the authors “do think that the atmospheric conditions in summer in the Arctic are comparable to those in winter in the Netherlands ”. I don’t think so. Surface temperature are close to zero over ice and surface-atmosphere interactions are different
Meanwhile, we reprocessed the MWR data with an retrieval that was created by University of Cologne for the location of Ny Alesund (78.9°N, 11.8°E). We mention this in the file diff.pdf in lines 140-145. The data will also be uploaded as a new version to Pangaea. Same holds for the depending Cloudnet-processed dataset on Pangaea. Fig. 1

shows the correlation of the two datasets. Overall, the correlation is quite linear, especially for the IWV/PRW. Only in the low-LWP range <100 g/m², considerable relative biases can be found.

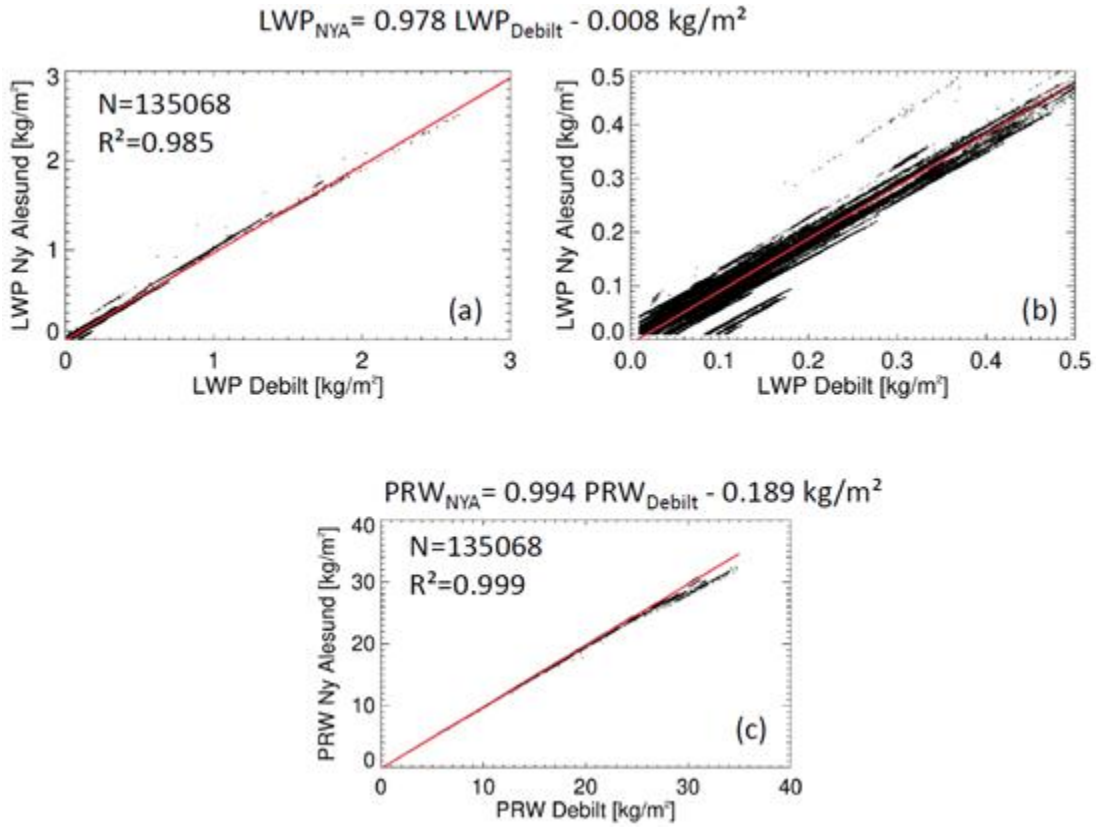

Fig. 1: Comparison of LWP (a, b) and IWV/PRW (b) derived from (unflagged) MWR observations with retrievals from De Bilt and Ny Alesund.

Page 7, Table 1 : Add information on the auxiliary measurements (tethered balloon, sonic anemometer, pyranometers, ...)
Done

Page 8, Figure 3 legend : extend period limits on the vertical with dotted lines
Done

Page 10, Figure 5: put the histograms outside the figure so to better see the full 2D plot
Done

Page 10, line 194 to 246 : Extend discussion on error induced by the correction. What is the expected in terms of residual contribution ? What bias is to be considered in the sigma correction, and error induced as an additional error. This can be discussed from the spectrum shape, errors and confidence in the limits of analysis to be used. Present/discuss more in detail the corrected spectrum in section versus non-corrected one and versus the sonic anemometer one.
We have extended the discussion and used the Fourier analysis to further quantify the effect of the heave correction. See lines: 226-230

Page 11, line 230 : typo vertical
Corrected

Page 12, Figure 6 shows linearized fit from sonic only, what would be the one from corrected spectrum ? Discuss values retrieved from the range of the fit identified from the residual errors and confidence in the correction.
We added the spectrum for both cloud radar Doppler velocity and sonic. Also we calculated the standard deviation of all good fits to estimate the uncertainty of the approach. See lines: 271-281, Fig. 7.

Page 12, Figure 6 legend : refers to values of EDR, but hypotheses for deriving EDR from radar should be more discussed (see above).
First, we have removed the subfigure 6(b) as suggested by Reviewer 2. Concerning the approach of EDR retrieval from radar data, we provide an extensive introduction to the topic in Section 3.2.1 and lines 253-272.

Page 12, line 251 : Iacono et al., 2208, is not a general reference for RRTMG. This ref is to be replaced by a more appropriate one.
We replaced the reference by Mlawer 1997, Barker 2003 Clough 2005. See line 294.

Page 13, line 288 : It is OK here, but more generally for Arctic clouds I am not sure of that, as for supercooled precipitating clouds
We removed the respective sentence about liquid water attenuation. See line 346.

Page 14, line 310 : a strong attenuation
Done

Page 14, line 318 : I would suggest to use scattering ratio Sr as well, which would further allow to discuss fog issue using lidar measurements only assuming a threshold in Sr
Dealing with lidar signals in the very near range (below 300m) is bound to the presence of technical caveats. Mainly, it is the incomplete overlap of the receiver-field-of-view and the laser beam. Derivation of physical values, such as SR or att. BSC, from single-channel elastically backscattered light is thus impossible very close to the ground, even for the near-range channels of PollyXT (complete overlap at 120 m). We thus decided to rely on the utilization of the technical value SNR for the detection of the cloud layers below 50 and 160 m height, which delivers very good results.

Page 15, line 348 : I would suggest to extend presentation here and discuss meteorological context change to introduce cases studies and overall meteorological patterns observed leading to the various cases analyzed. I would suggest to move Figure 11 here and briefly discuss more general transport evolution over the period studied (not necessarily adding a figure).
We added an introduction to the overall synoptic situation based on Knudsen et al (2018) who gave a synoptic overview of the PS106 campaign. See lines: 415-422.

Page 20, Figure 10 : I would suggest to present lidar scattering ratio instead of backscattering coefficient (to better support aerosol/fog/cloud discrimination).
The provided attenuated backscatter coefficient is a standard product of the Polly-XT processing chain (Baars et al., 2017). We thus would like to keep this parameter presented in Fig. 12 (version of Figure 10 from before the revision), as it is the default lidar parameter in Cloudnet and as we show it as standard parameter in other publications.

Page 23, and 24 : Synergies between the remote sensing instruments and auxiliary observations from aboard Polarstern were analyzed by means of Cloudnet classification procedure. This procedure is shown to induce caveats because of limitations in the radar range measurements. More discussions on the way this could be mitigated using lidar measurements should be included.

We extended the discussion of the caveats of Cloudnet and our approach to address them with the lidar measurements. See lines 366-386.

Page 23, lines 429-432 : PollyXT "Though detected fog almost continuously during the case study, : : :". How is this done ? Explain in the text how this can be translated in an additional information below 165 m in a quantitative way from scattering ratio.

As also pointed out by Reviewer #2, the terminology 'fog' is indeed inappropriate to describe what we intend to detect. We thus renamed the 'fog' flag to 'low level stratus clouds'. This better describes that we aim with our approach on detecting clouds which are (1) located above the visibility sensor of Polarstern and (2) located below the good-performance-range of the ceilometer CL51 (deployed on Polarstern). The Figure below (Fig. 2) demonstrates this approach and the advantages. Figure 2 (a-d) present cloud parameters as derived from the CL51 ceilometer observations aboard Polarstern during the time period from 07 Jun 2017, 21 UTC to 08 Jun 2017, 09 UTC. Figure 2 (e) shows the combined Cloudnet (>165 m) and PollyXT-based (<165 m height) cloud masks and periods of fog (horizontal blue lines) as derived from the on-board visibility sensor of Polarstern (which is Figure 17 in the manuscript). Figure 2(f) shows the liquid water path as measured by the microwave radiometer HATPRO of OCEANET. The figure demonstrates nicely the situation that frequently occurred: Almost for the whole time period, CL51 shows a cloud deck, confirming that there were actually clouds present. However, the reported cloud base is continuously above 150 m height during most of the time. Even when the visibility sensor indicated fog (22:00-23:30 UTC on 7 June), the ceilometer cloud base was > 200 m. The ceilometer also reports clouds at heights, where the combined lidar + cloud radar cloud mask from Cloudnet does not show any clouds at all. This is especially visible in the time period from 05-08 UTC on 8 June. This means, that the actual cloud base must have been located lower than the lowest height of Cloudnet. And this is when the lidar data of PollyXT is of help: The threshold of SNR>40 provides a good and reasonable estimate of the actual cloud boundaries at heights <165 m.

We decided to not do a detailed discussion of the issues of the CL51 within the manuscript. However, from our observations it is clear, that the reported cloud bases from the CL51 are continuously too high, at least in situations with very low clouds present. We hope that Figure 2 demonstrates well to the referees that the new cloud mask from PollyXT is valuable. The cloud mask will also be published in Pangaea to provide other users a good estimate of the low-cloud occurrence - a very important parameter for the radiative and water balances.

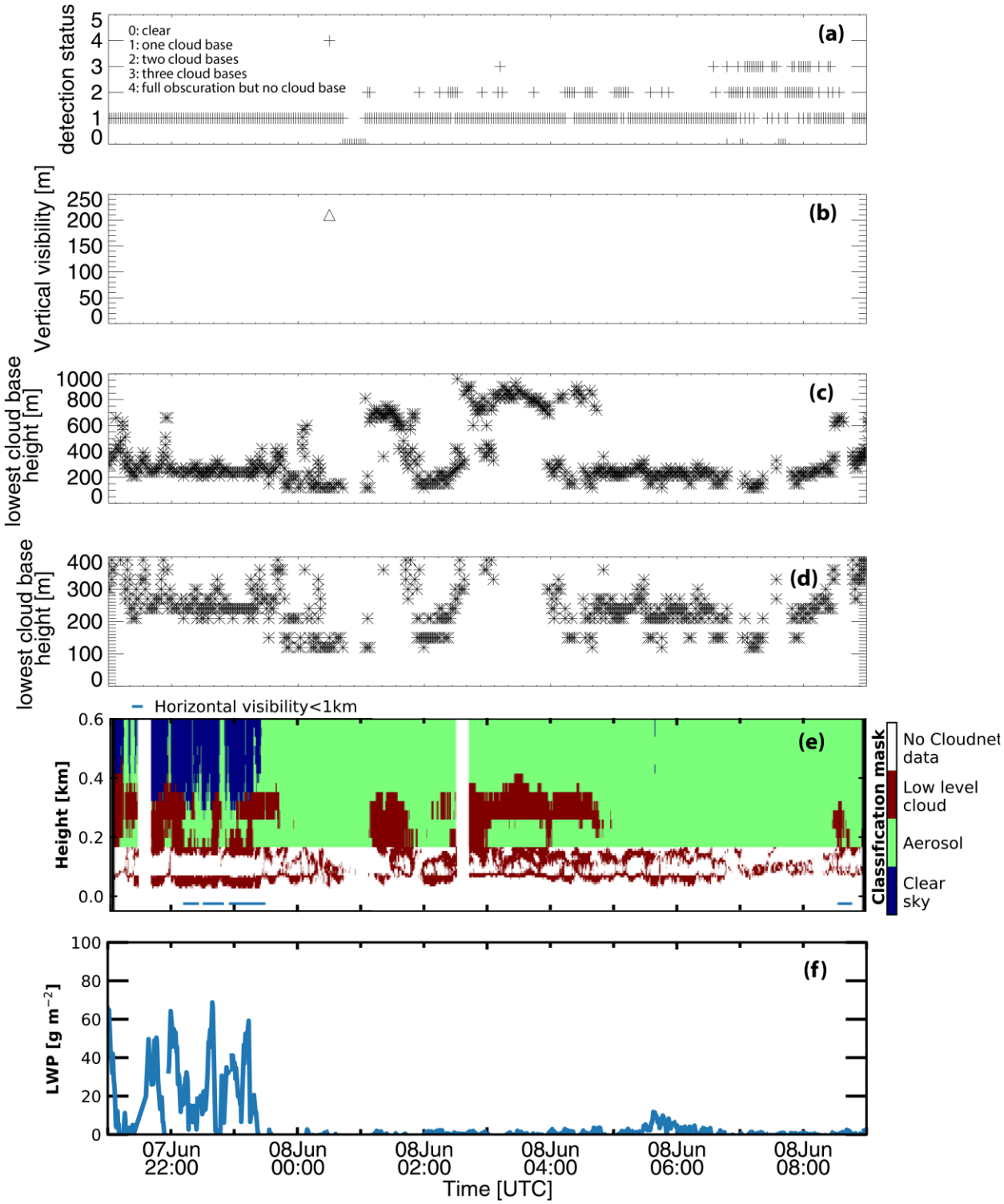

Fig. 2: Comparison of ceilometer-derived cloud bases, PollyXT 'low stratus' detection mask and visibility sensor for the Polarstern observations from 07 Jun 2017, 21 UTC to 08 Jun 2017, 09 UTC. (a) detection Status of the CL51 Ceilometer; (b) vertical visibility from CL51 (if detection status equals 4); (c) and (d) height of lowest cloud base from CL51; (d) Cloudnet cloud and aerosol mask (above 165 m), PollyXT low-level stratus mask (below 165 m) and fog-periods

(horiz. blue lines) as derived from the visibility sensor. (f) liquid water path as derived from the microwave radiometer HATPRO.

Page 24, Figure 15 : Blue color below 165 m shows occurrence of clear air <165m. It is thus misleading as no information is available from Cloudnet. Should be another color corresponding to unknown (white?) instead of blue below 165 m in Fig 15. Could be replaced by dots corresponding to fog color on a white background from the discussion on fog detection by lidar only.
Done

Page 24 line 435 : “above the fog layer” meaning well above !
Changed ‘above’ to ‘well above’.

Page 28, lines 509-510 : Yes, frequently observed from surface-based IAOOS observations as reported in Mariage et al., 2016
We included their findings in our discussion, lines 603-605.

Authors response - AMT

Application of the shipborne remote sensing supersite OCEANET for profiling of Arctic aerosols and clouds during Polarstern cruise PS106 – Griesche et al.

Response to Anonymous Referee #2 (22 January 2020)

We would like to thank the Anonymous Referee #2 for dedicating time in order to improve the manuscript and giving help by providing us with valuable comments and suggestions. We have revised the initial submission, and hope that the manuscript is now acceptable for publication.

Our point-by-point response to the review comments is written here in bold font. The marked-up manuscript version with all changes compared to the initial submission is attached to this file and its line numbering is used to reference changes below.

Overall summary of major changes:

We would like to inform the referee about the following major changes:

- **Revision of the abstract due to suggestion of Referee #2**
- **Reprocessing of the Cloudnet data with an Arctic MWR-retrieval considering the comments of both Referees #1 and #2**
- **Included a better evaluation of the capability of the motion stabilization according to comments by both Referees #1 and #2**
- **Improved the discussion of the eddy dissipation rate and fog/low-level stratus retrievals as well as Cloudnet in general considering the comments by both Referee #1 and #2**

Detailed responses:

The authors describe the deployment of the Oceanet remote-sensing container during a cruise to the Arctic. Right now it is not clear if the authors want to present technical development or research findings. The authors briefly describe a new motion stabilisation platform and a new data processing method for fog detection. However, they fail to provide a validation that those are working. The remainder of the paper is dedicated to case studies. The paper is of interest to the community but needs major revisions. First of all, the authors need to make up their mind if this should be a paper for AMT or ACP. There are further major items that need to be addressed before it can be considered for publication:

- [Abstract] The Abstract appears to be more of an introduction than a concise summary of the paper. Key points of the article are missing. Please rewrite the Abstract.

We rewrote the paragraph in such a way that it provides a more concise summary (See lines 1-30).

- [MWR retrieval] One of the major issues with this work is related to the analysis of the microwave radiometer measurements. I do not agree with the assumption that atmo- spheric

conditions in the Arctic are comparable with those during winter in the Nether- lands. In the Netherlands the minimum temperature rarely reaches 0◦C; also radiative balance is not comparable. The analysis needs to be repeated with a customised Arctic retrieval. Radiosonde data can be obtained from several research cruises in the Arctic since 1990 and are also available from research stations around the Arctic.

Meanwhile, we reprocessed the MWR data with an retrieval that was created by University of Cologne for the location of Ny Alesund (78.9°N, 11.8°E). We mention this in the file diff.pdf in lines 140-145. The data will also be uploaded as a new version to Pangaea. Same holds for the depending Cloudnet-processed data set on Pangaea. Fig. 1 shows the correlation of the two data sets. Overall, the correlation is quite linear, especially for the IWV/PRW. Only in the low-LWP range <100 g/m², considerable relative biases can be found.

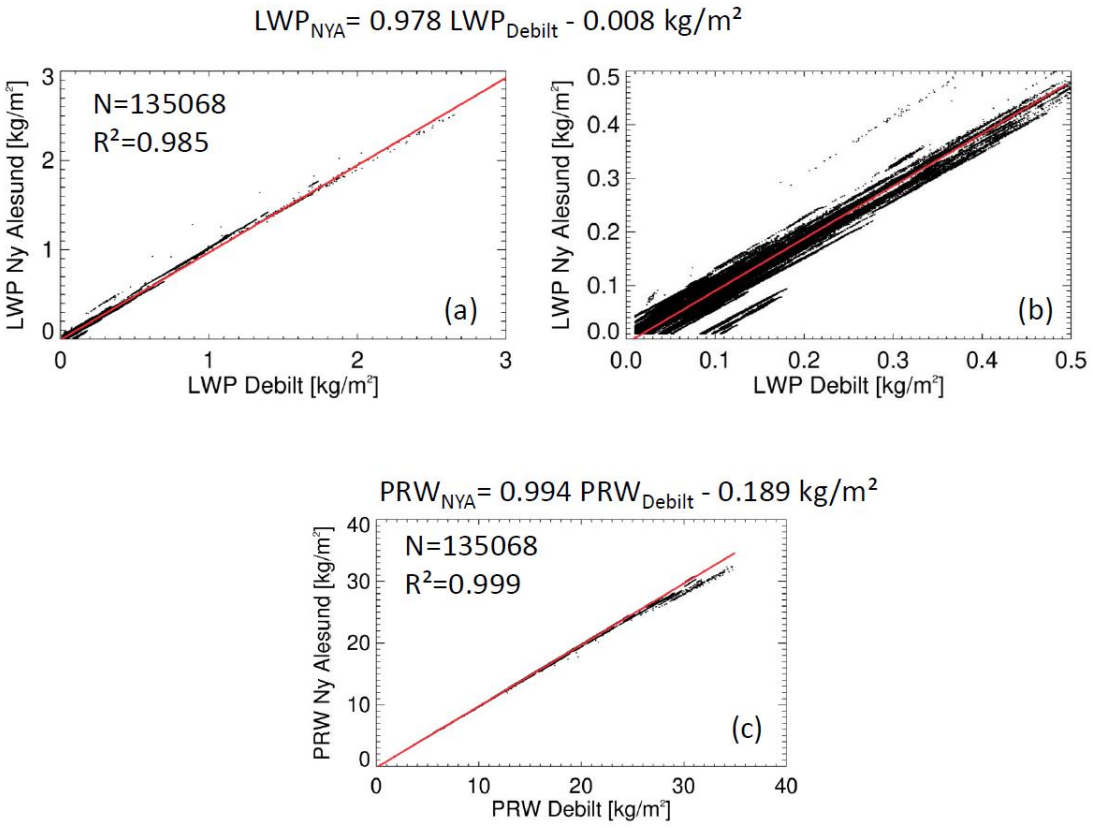

Fig. 1: Comparison of LWP (a, b) and IWV/PRW (b) derived from (unflagged) MWR observations with retrievals from De Bilt and Ny Alesund.

- [Motion stabilisation] The authors should provide proof that the roll and pitch was actively levelled out for the motion-stabilised radar measurement. Please provide a time series of roll angles for the ship and radar during roughest sea and the probability distribution of radar roll angle for at least a 1 h period with greatest ship roll. Further information on the measurement conditions is needed to assess the performance of the motion stabilisation platform. What was

the maximum roll angle? What was the ship's mean horizontal velocity when underway? What was the wave-induced velocity perturbation in open water?

The discussion of the motion stabilization and its influence on the measurements has been improved. We have compared the pitch and roll movement of the Polarstern to the respective measurements of a small single board computer (Beaglebone Blue) mounted on the cloud radar during different periods of the campaign. From the comparison, we conclude that the stabilization was challenging when RV Polarstern cruised through open waters. Under these conditions, the vertical pointing accuracy could be reduced to within 1° off-zenith. While breaking through the ice and during the ice-floe period, the platform stabilized the vertical pointing with an accuracy of 0.5°.

See lines: 196-202, 566-575, Figure 4.

The heave correction was further analyzed and quantified by investigating the Doppler velocity spectrum of the corrected and uncorrected Doppler velocity. The applied heave correction reduced the signal induced by the vertical movement of the cloud radar in the power spectral density of the Doppler velocity by a factor of 15.

See lines: 226-230, Figure 6.

- [Eddy dissipation rate] The validation of eddy dissipation rate is not convincing. At what height was the tethered balloon located? Below a cloud or within a cloud? What are the reasons for the over- and underestimation? Also, it would be good to have more than two comparisons cases between the Radar and the measurements with the tethered balloon or to provide justification why this is not done. Please also provide the ÉZ˙ values from tethered balloon and radar for both cases.

We have extended the discussion on the EDR retrieval and included additional information, like the height of the tethered balloon, in the manuscript. The standard variation of the derived EDR values has been calculated to better evaluate the retrieved values. We also added another comparison of EDR between the cloud radar and the tethered balloon. Adding more comparisons is not possible as the measurement strategy of the balloon was not only focused on clouds and therefore no more co-located observations are available.

See lines: 271-289, 574-580.

- [Cloudnet and cloud definition] There are several issues related to the Cloudnet retrieval. Right now it is often unclear what has been done. For instance, the description of the classification mask (Page 13, line 261) does not agree with the shown Cloudnet target classification in Figure 9a. Please provide more details on Cloudnet in general and on the classification mask and the target classification for readers that are not fa- miliar with the method. Further, it is not clear if the presented definition of liquid and mixed-phase clouds (page 12, second paragraph) is an official Cloudnet product such as the target classification or if it is a new data product developed by the authors. In that context, why not use the target classification as in comparable studies based on multi-sensor retrievals? In those, Arctic mixed phase clouds are defined when both liquid/supercooled water and ice particles are present and when ice particles are identified directly below liquid and mixed-phase regions (e.g. Shupe 2011, Mioche et al. 2015). For

comparison of cloud statistics from different campaigns it is important to use the same definition as already used in the literature.

We agree with the reviewer that the Cloudnet retrieval has certain caveats. This study presents a calibrated data set of measurements, which is suitable for synergistic retrievals such as Cloudnet. To provide comparable statistics to other retrievals the data set should be processed with the respective retrieval. We adapted our introduction of Cloudnet to the simpler classification mask, which is based on the categorization bits. This classification mask is used in the manuscript in Figures 11(a) and 16(a).

The differentiation between supercooled liquid clouds and mixed-phase clouds at a temperature right below 0°C remains difficult. In the mentioned Figure, a cloud radar pixel was detected right below the cloud. In this situation, it is not possible with present remote sensing methods to differentiate between ice and supercooled liquid. This is only done by dew point temperature. In this case, the cloud top temperature was very close to 0°C and supercooled liquid has been found in Arctic stratiform clouds down to -4°C (Zhang et al., 2017).

See lines: 305-337

- [Fog detection] The information related to the fog detection is not adequate to evaluate if the proposed method works. Please make use of the visibility sensor aboard Polarstern to assess your findings as well as to test if your assumed SNR value of 40 can be used to reliably detect fog. Just as a reminder, fog is defined when the visibility is below 1 km. The visibility sensor can also be used to distinguish between fog and low clouds. In that regard, please compare the detected low cloud layers with the observation of the ceilometer aboard Polarstern. The first height bin is much lower than the first height bin of the Polly system. Also would it not be better to use the ceilometer for detection of fog and low cloud layers? First of all the first cloud layer is lower and the Ceilometer on Polarstern is a CL51 which reports the vertical visibility in case that the lowest height bins are obscured due to precipitation and/or fog?

We decided to change our naming and to call our new product low-level stratus cloud instead of fog. This is closer to reality as the Polly system is only able to observe clouds starting from a height of >50m. To assess whether the SNR of 40 is a reasonable, we made a comparison between the low-level stratus cloud occurrence using three different SNR thresholds in addition to the occurrence of fog by means of the horizontal visibility sensor from Polarstern. Figure 2 shows this comparison. In blue (green) the low stratus occurrence due to a SNR of 20 (60) is indicated. Orange shows the original findings with the SNR of 40. The dashed red lines shows the frequency of occurrence of horizontal visibility below 1 km. The SNR value of 40 was manually found to provide the best visual correlation with the visibility measurements as well as to signatures of signal attenuation in the time-height cross-sections of the Cloudnet attenuated backscatter coefficient and HATPRO LWP measurements (see, e.g., Fig. 4 of this reply letter or Figs. 10 and 14 in the

manuscript).

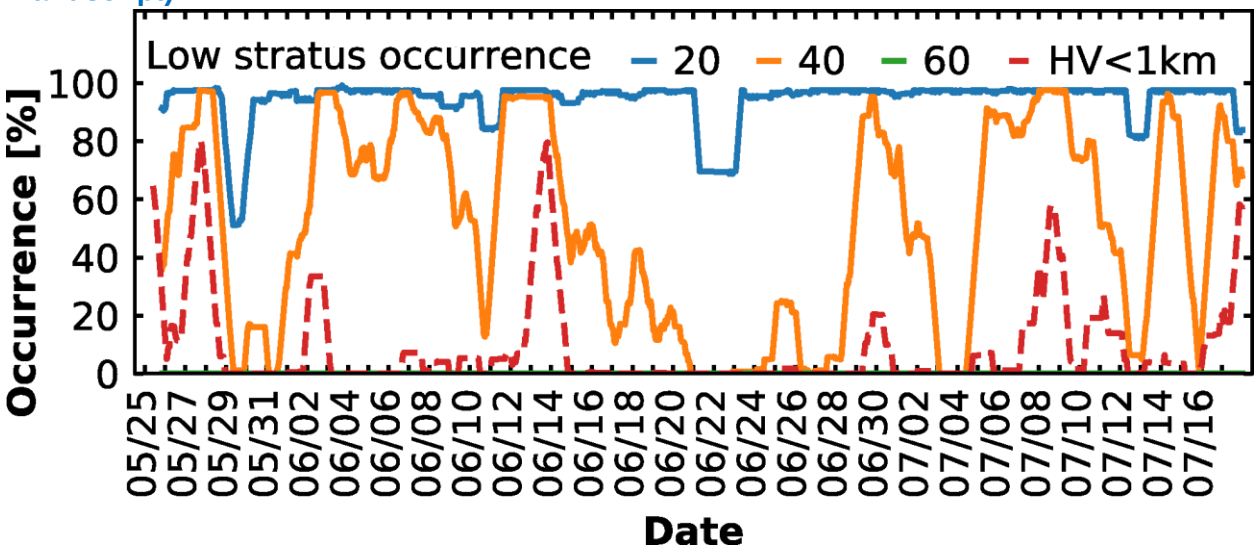

Fig. 2: Comparison of low stratus occurrence due to a SNR of 20 (blue), 40 (orange) and 60 (green) and visibility below 1 km (HV, dashed red).

See lines: 366-386

Minor issues

- Line 88, Please also cite Ehrlich et al. (2019) for ACLOUD
Done

- Line 122: It is not clear if only winter time radiosondes from De Bilt are used in the retrieval. Please clarify. But even better would be to revise the retrieval using actual Arctic measurements.
We used a retrieval the location of Ny Alesund. See answer to major comment above.

- Line 126: An Arctic retrieval based on ERA-Interim data should be compared to a retrieval based on Radiosonde data. Systematic errors in ERA-Interim data (e.g. Wesslén et al., 2014, for temperature bias) can have an influence on the MWR retrieval. Consider using ERA5 instead.
We used a retrieval the location of Ny Alesund. See answer to major comment above.

- line 153: Please provide the typical error range of the RS92 measurements
Done

- line 270: Do you mean T or Td (dew point temperature here).
We deleted this paragraph (but Td was meant).

- line 344: Can you please verify if the mixing depth provided by GDAS1 is comparable to the observed mixing depth. It is known that models have problems to provide realistic mixing depth in the Arctic.

We have removed the mixing depth analysis provided by trace from the study. Nevertheless, we provide ensemble trajectories in Figure 8. There it is well demonstrated that approximately 50% of the ensemble trajectories passed the European continent where they were involved in boundary layer processes, as indicated by the PBLH values of the underlying GDAS1 data.

- line 354: Do you mean Figure 4.1.1? And the profiles are shown to a height of 2.5 km not 2.0 km.
Indeed, we wanted to refer to (old) Figure 4.1.1. We changed the text also to 2.5km.

- line 356: Since ice particles are below the liquid stratocumulus the cloud should be reclassified as mixed-phase cloud (see major comments).
We agree that this is an ambiguous cloud situation. Still we rather stick with liquid or liquid-dominated cloud. See also answer to major comment on the Cloudnet retrieval.

- line 375: As observed by Shupe et al. (2013). Please add citation.
Done

- The figures do not appear in the order they are discussed in the text. Please revise.
Done

- Figure 6b is not necessary and should be omitted.
Figure 6b has been removed.

- Figure 15: Fog and low cloud should have different colours. Again use the visibility sensor to distinguish between fog and low clouds. Add visibility to the plot. Also add the observed backscatter from the CL51 as comparison as an extra plot next to it.
As also pointed out by Reviewer #1, the terminology 'fog' is indeed inappropriate to describe what we intend to detect. We thus renamed the 'fog' flag to 'low level stratus clouds'. This better describes that we aim with our approach on detecting clouds, which are (1) located above the visibility sensor of Polarstern and (2) located below the good-performance-range of the ceilometer CL51 (deployed on Polarstern). The Figure below (Fig. 4) demonstrates this approach and the advantages. Figure 4(a-d) present cloud parameters as derived from the CL51 ceilometer observations aboard Polarstern during the time period from 07 Jun 2017, 21 UTC to 08 Jun 2017, 09 UTC. Figure 4(e) shows the combined Cloudnet (>165 m) and PollyXT-based (<165 m height) cloud masks and periods of fog (horizontal blue lines) as derived from the on-board visibility sensor of Polarstern (which is Figure 17 in the manuscript). Figure 4(f) shows the liquid water path as measured by the microwave radiometer HATPRO of OCEANET. The figure demonstrates nicely the situation that frequently occurred: Almost for the whole time period CL51 shows a cloud deck, confirming that there were actually clouds present. However, the reported cloud base is continuously above 150 m height during most of the time. Even when the visibility sensor indicated fog (22:00-23:30 UTC on 7 June), the ceilometer cloud base was >200 m. The ceilometer also reports clouds at heights, where the combined lidar + cloud radar cloud mask from Cloudnet does not show any clouds at all. This is especially visible in the time period from 05-08 UTC on 8 June. This means, that the actual cloud base must have been located lower than the lowest height of Cloudnet. And this is when the lidar data of PollyXT is of help: The threshold of SNR>40 provides a good and reasonable estimate of the actual cloud boundaries at heights <165 m .
We decided to not do a detailed discussion of the issues of the CL51 within the manuscript. However, from our observations it is clear, that the reported cloud bases from the CL51 are continuously too high, at least in situations with very low clouds present. We hope

that Figure 4 demonstrates well to the reviewers that the new cloud mask from PollyXT is valuable. The cloud mask will also be published in Pangaea to provide other users a good estimate of the low-cloud occurrence - a very important parameter for the radiative and water balances.

- Figure 17: How is fog height determined? That needs to be discussed in 3.3.3. Add visibility to the plot.
The low level stratus height was determined by the lowest and the highest PollyXT pixel of the low level stratus mask, which exceeded the SNR-threshold (also mentioned in the manuscript in lines 385-386). We added a flag to indicate periods of horizontal visibility < 1 km in Figure 17.

- line 500, e.g. Sotiropoulou et al. (2014) and (2016) considered low clouds from ceilometer/Halo and radar measurements.
We have considered their findings in our discussion.

- Line 762: Somag, the provided link does not work. Please provide an open link or add the information to the text.
Done

- Figures 7, 10 (upper panel), and 13: Please use same scale for T and RH in all plots.
Done

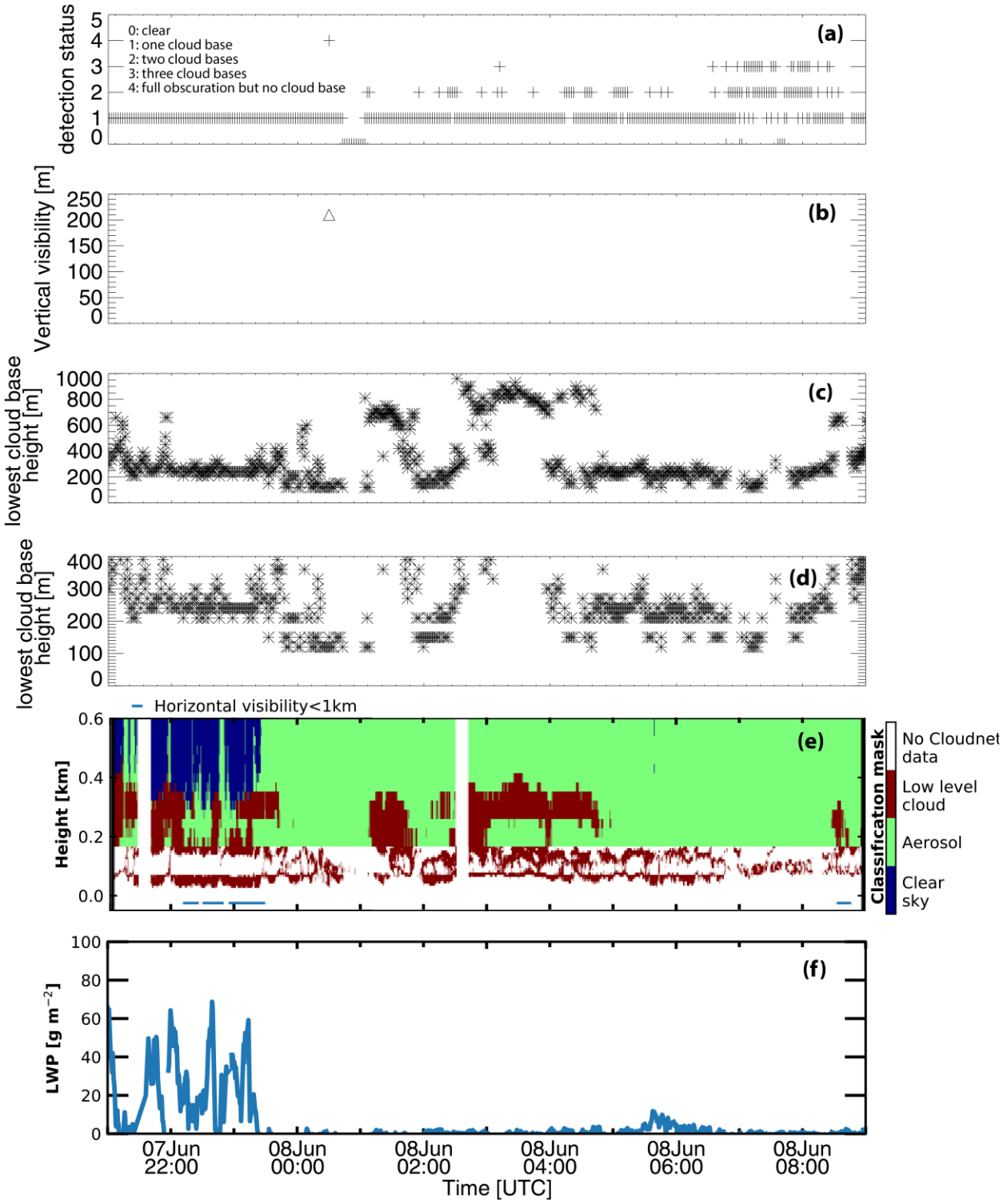

Fig. 4: Comparison of ceilometer-derived cloud bases, PollyXT 'low stratus' detection mask and visibility sensor for the Polarstern observations from 07 Jun 2017, 21 UTC to 08 Jun 2017, 09 UTC. (a) Detection Status of the CL51 Ceilometer; (b) vertical visibility from CL51 (if detection status equals 4); (c) and (d) height of lowest cloud base from CL51; (d) Cloudnet cloud and aerosol mask (above 165 m), PollyXT low-stratus mask (below 165 m) and fog-periods (horiz.

blue lines) as derived from the visibility sensor. (f) liquid water path as derived from the microwave radiometer HATPRO.

References:

Ehrlich, A., Wendisch, M., Lüpkes, C., Buschmann, M., Bozem, H., Chechin, D., . . . Zanatta, M. (2019). A comprehensive in situ and remote sensing data set from the Arctic CLoud Observations Using airborne measurements during po- lar Day (ACLOUD) campaign. Earth System Science Data Discussions, 1–42. https://doi.org/10.5194/essd-2019-96

Wesslén, C., Tjernström, M., Bromwich, D. H., De Boer, G., Ekman, A. M. L., Bai, L. S., & Wang, S. H. (2014). The Arctic summer atmosphere: An evaluation of re- analyses using ASCOS data. Atmospheric Chemistry and Physics, 14(5), 2605–2624. https://doi.org/10.5194/acp-14-2605-2014

Shupe, M. D.: Clouds at Arctic Atmospheric Observatories, Part II: Ther- modynamic phase characteristics, J. Appl. Meteor. Clim., 50, 645–661, doi:10.1175/2010JAMC2468.1, 2011.

Mioche, G., Jourdan, O., Ceccaldi, M., and Delanoë, J.: Variability of mixed- phase clouds in the Arctic with a focus on the Svalbard region: a study based on spaceborne active remote sensing, Atmos. Chem. Phys., 15, 2445–2461, https://doi.org/10.5194/acp-15-2445-2015, 2015.

Shupe, M. D., Persson, P. O. G., Brooks, I. M., Tjernström, M.,Sedlar, J., Mauritsen, T., Sjogren, S., and Leck, C.: Cloud and boundary layer interactions over the Arctic sea ice in late sum-mer, Atmos. Chem. Phys., 13, 9379–9399, doi:10.5194/acp-13-9379-2013, 2013.

Sotiropoulou, G., Sedlar, J., Tjernström, M., Shupe, M. D., Brooks, I. M., and Pers- son, P. O. G.: The thermodynamic structure of summer Arctic stratocumulus and the dynamic coupling to the surface, Atmos. Chem. Phys., 14, 12573–12592, https://doi.org/10.5194/acp-14-12573-2014, 2014.

Sotiropoulou, G., Tjernström, M., Sedlar, J., Achtert, P., Brooks, B. J., Brooks, I. M.,

Wolfe, D. (2016). Atmospheric conditions during the Arctic clouds in summer experi- ment (ACSE): Contrasting open water and sea ice surfaces during melt and freeze-up seasons. Journal of Climate, 29, 8721-8744

Application of the shipborne remote sensing supersite OCEANET for profiling of Arctic aerosols and clouds during Polarstern cruise PS106

Hannes J. Griesche, Patric Seifert, Albert Ansmann, Holger Baars, Carola Barrientos Velasco, Johannes Bühl, Ronny Engelmann, Martin Radenz, and Yin Zhenping

Leibniz Institute for Tropospheric Research (TROPOS), Leipzig, Germany

Correspondence: Hannes Jascha Griesche (griesche@tropos.de)

Abstract.

From 25 May to 21 July 2017, the research vessel Polarstern performed the cruise PS106 to the high Arctic in the region north and northeast of Svalbard. ~~PS106 contributed observations for the initiative "Arctic Amplification: Climate Relevant Atmospheric and Surface Processes and Feedback Mechanisms (AC)^3" which involves numerous projects aiming on understanding the role of atmospheric and surface processes in the ongoing rapid changes in the Arctic climate. As one of the central facilities of (AC)^3, the~~ The mobile remote sensing platform OCEANET was deployed aboard Polarstern. Within a single container, OCEANET houses state-of-the-art remote sensing equipment, including a multi-wavelength Raman polarization lidar Polly^{XT} and a 14-channel microwave radiometer HATPRO. For the cruise PS106 the measurements were supplemented by a motion-stabilized 35-GHz cloud radar Mira-35.

~~This paper~~ This article describes the treatment of technical challenges which were immanent during the deployment of OCEANET in the high Arctic. This includes the description of the motion stabilization of the cloud radar Mira-35 to ensure vertical-stare observations aboard the moving Polarstern ~~. Also, low-level clouds and the presence of fog~~ as well as the applied correction of the vessels heave rate to provide valid Doppler velocities. The correction ensured a leveling accuracy of $\pm 0.5°$ during transits through the ice and a performed ice floe camp. The applied heave correction reduced the signal induced by the vertical movement of the cloud radar in the PSD of the Doppler velocity by a factor of 15. Low-level clouds in addition frequently prevented a continuous analysis of cloud conditions from synergies of lidar and radar within Cloudnet, because the technically determined lowest detection height of Mira-35 was 165 m above sea level. To overcome this obstacle, an approach for identification of the cloud presence solely based on data from the near-field receiver of Polly^{XT} at heights from 50 m and 165 m above sea level is presented. We found low level stratus clouds, which were below the lowest detection range of most automatic ground-based remote sensing instruments during 25% of the observation time.

~~In addition, we provide an overview of the data processing chain of the OCEANET observations and demonstrate~~ We present case studies of aerosol and cloud studies to introduce the capabilities of the ~~dataset. The~~ data set. In addition, new approaches for ice crystal effective radius and eddy dissipation rates from cloud radar measurements and the retrieval of aerosol optical and microphysical properties from the observations of Polly^{XT} ~~is presented by means of observations performed during the ice floe camp. Synergies between the remote sensing instruments and auxiliary observations from aboard Polarstern were analyzed~~

by means of Cloudnet which provides as primary output a target classification mask. This target classification is the basis for value-added products such as liquid- and ice-cloud microphysical properties, cloud dynamics which can in subsequent steps be used as input for the investigation of cloud microphysical processes, radiative transfer calculations, or model evaluation. To this end, new approaches for ice crystal effective radius and eddy dissipation rates have been implemented into Cloudnet. are introduced.

1 Introduction

The Arctic is one of the hot spots of global climate change. This is observed as a change of several parameters such as the drastic decline of the Arctic sea ice during all seasons, but especially in summer, in both extend and thickness (Meier et al., 2014). Also, in the past 30 years the mean Arctic near surface air-temperature anomaly increased at least by a factor of two faster compared to the global mean (Serreze and Barry, 2011). These phenomena, also summarized by the term Arctic Amplification, are assumed to be due to several feedback mechanisms, e.g., the surface albedo feedback, lapse rate feedback, a change in the meridional atmospheric and oceanic mass and energy transport pattern, and an alteration in cloud cover, aerosol occurrence, and atmospheric moisture content (Wendisch et al., 2017). However, there is still a lack of understanding in the interplay of these feedback mechanisms as well as in quantifying their relative importance and magnitude (Serreze and Barry, 2011; Pithan and Mauritsen, 2014; Goosse et al., 2018).

The radiative effect of clouds is a major source of uncertainty in this matter. Arctic clouds have a high variability in their radiative effects and in their impact on the surface energy balance (Yeo et al., 2018). The cloud-related radiative impacts have been found to be both positive (i.e., clouds have a warming effect) as well as negative (Goosse et al., 2018). A higher fraction of low clouds, e.g. caused by a decreased sea ice extent, increases the downwelling longwave radiation during polar night and thus induces a positive feedback. A higher fraction of liquid water in mixed-phase clouds due to a warmer climate, on the other hand was found to increase the cloud albedo. This in turn enhances the reflection of incoming shortwave radiation at the top of the atmosphere during polar day (Goosse et al., 2018) and thus produces a negative feedback. Yet the underlying processes controlling Arctic cloud phase and occurrence, and hence the connected feedback mechanisms driving Arctic Amplification are not completely understood (e.g., Shupe et al., 2013; Kalesse et al., 2016a).

Though being a key requirement to study the Arctic energy budget, detailed observations of Arctic clouds still are rare. To study these Measurements from ground based stations, such as the observatories of the International Arctic Systems for Observing the Atmosphere (Uttal et al., 2016) are of great value, e.g. due to their possibilities of conducting long-term observations. However they are limited to their location and influenced by their surrounding orography. Drifting buoys on the other hand can enter any place in the Arctic ice and thus are very valuable in this harsh environment. Their equipment gets increasingly sophisticated and since a few years buoys equipped with autonomous lidar systems (Mariage et al., 2017) have been in use, giving them the opportunity to measure vertical profiles of the atmospheric column. But they still are limited in their payload and can not yet replace measurements from observatories or campaigns. To study Arctic clouds, different aircraft campaigns have been conducted in recent years in the Arctic (e.g., Curry et al., 2000; Jacob et al., 2010; McFar-

quhar et al., 2011; Wendisch et al., 2019). While airborne measurements yield an unique, accurate description of the observed cloud, they lack the ability to measure continuously the entire tropospheric column ~~at once. This is a feature which~~ over a long period, a feature active remote sensing observations can offer. Given this capability, ground-based remote sensing observations are suitable to investigate the spatio-temporal distribution of clouds (Bühl et al., 2013), their phase partitioning (de Boer et al., 2009; Zhang et al., 2014; Kalesse et al., 2016a), and their interaction with aerosols (Seifert et al., 2010). These data sets serve, e.g., as basis for model evaluation (Illingworth et al., 2007; Neggers, 2019) and radiative transfer calculations ~~(Barrientos Velasco et al., 2019; Ebell et al., 2019)~~(Ebell et al., 2019; Barrientos Velasco et al., 2020). Hence, additionally to the airborne campaigns, several shipborne campaigns equipped with remote sensing instrumentation have been conducted in the past years in the Arctic (e.g., Uttal et al., 2002; Tjernström et al., 2004; Tjernström et al., 2014; Granskog et al., 2018; Wendisch et al., 2019). Observations of space-borne cloud radar and lidar, as done aboard Cloudsat (Stephens et al., 2008) and CALIPSO ~~(Winker et al., 2003)~~ (Winker et al., 2010) provide in addition a large-scale overview of the Arctic cloud coverage (Liu et al., 2012). But the respective data sets lack information about the lowest cloud levels. Nevertheless, there are still only a few studies of sea-motion-stabilized cloud radars, whose availability is a necessary requirement to determine also cloud vertical dynamics accurately from a shipborne platform.

In order to study the feedback mechanisms causing Arctic Amplification, the initiative **A**rcti**C** **A**mplification: **C**limate Relevant Atmospheric and Surfa**C**e Processes and Feedback Mechanisms $(AC)^3$ conducted two complementary field campaigns in the Arctic summer of 2017: **A**rctic **CL**oud **O**bservations **U**sing airborne measurements during polar **D**ay (ACLOUD), an airborne campaign performed with the research aircraft Polar 5 and Polar 6, and the **P**hysical feedbacks of **A**rctic boundary layer, **S**ea ice, **C**loud and **A**eroso**L** (PASCAL) expedition deployed on and around the research ice breaker Polarstern (Macke and Flores, 2018; Wendisch et al., 2019). These campaigns took place in May and June 2017 in the regions north and northeast of Svalbard with the aim to combine remote sensing and in-situ observations. During PASCAL, a two-week ice floe camp was performed in the vicinity of Polarstern and a large number of auxiliary measurements were conducted on the ice. PASCAL was the first part of the split Polarstern cruise PS106 which ~~lasted~~ took place from 25 May until 21 July 2017. During the whole PS106 cruise, measurements with the multiwavelength polarization lidar Polly^{XT}_OCEANET, a 35-GHz cloud radar Mira-35 and a microwave radiometer HATPRO (**H**umidity **A**nd **T**emperature **PRO**filer) of the OCEANET platform were conducted aboard Polarstern. Within $(AC)^3$ the OCEANET observations have the essential role to describe the temporal evolution of the vertical structure of aerosol and clouds in the ~~Central~~ central Arctic. They constitute the prerequisite for further studies of aerosol-cloud interaction, model evaluation or radiative transfer modeling, which are partly covered by other subprojects of $(AC)^3$. Scope of this study is thus to introduce the instrumentation and data analysis methods which are used to produce the OCEANET-based cloud and aerosol data sets for the cruise PS106.

In Section 2 of this paper, a detailed description of the OCEANET instruments and the auxiliary observations is given. The applied motion stabilization and heave rate correction of the cloud radar Doppler velocity, the data processing based on the synergistic Cloudnet algorithm (Illingworth et al., 2007) and the development of auxiliary retrievals for processing within Cloudnet are described in Sect. 3. In Section 4 the products derived from the OCEANET measurements using Cloudnet are illustrated by means of different case studies from the time period of the ice flow camp. The potential of Polly^{XT}_OCEANET

to characterize the free-tropospheric aerosol is also highlighted. In addition, a statistical overview about the observed cloud vertical structure with a special focus on low-level clouds during PS106 is presented. A final summary and conclusions are given in Sect. 5.

2 Instrumentation

During the complete PS106 campaign in the central Arctic in summer 2017 (see Fig. 1) a comprehensive number of remote sensing instruments was deployed aboard the research vessel (RV) Polarstern to conduct continuous observations of clouds and ~~aerosol~~aerosols. To a large extent, these instruments were comprised in the OCEANET-Atmosphere observatory (Kanitz et al., 2013a). Additionally, auxiliary instruments for in-situ and remote sensing observations installed aboard Polarstern as well as during a two-week ice floe-camp, which was performed in the vicinity of the RV, were utilized for the studies presented in here. The first part of PS106 (PS106.1 / PASCAL) was accompanied by the ACLOUD aircraft campaign (Ehrlich et al., 2019) about both of which a brief overview is given by Wendisch et al. (2019).

The location of the OCEANET equipment and of the auxiliary Polarstern instruments deployed during PS106 that were used within this study are depicted in Fig. 2. Table 1 summarizes the technical details of the key equipment applied in the synergistic Cloudnet processing that is further described in Sect. 3.3. ~~The~~ In the following the different instruments will ~~in the following~~ be briefly introduced.

2.1 OCEANET

The OCEANET-Atmosphere observatory was already frequently operated aboard Polarstern ~~(Kanitz et al., 2013b).~~ (Kanitz et al., 2013b; Bohlmann et al., 2018; Yin et al., 2019). Yet, so far only for the transects from the northern to the southern hemisphere (or vice versa) but never in the Polar regions. Its container is by default equipped with the multi-wavelength polarization Raman lidar Polly^{XT}_OCEANET (hereafter referred to as Polly^{XT}), to provide continuous profiles of cloud and aerosol properties (Engelmann et al., 2016). Additionally, a 14-channel microwave radiometer (MWR) HATPRO (Rose et al., 2005) for measurements of column-integrated liquid water and water vapor content and profiles of atmospheric temperature, a standard meteorological station, a pyranometer and a pyrgeometer for incoming short- and longwave radiation observations, as well as an all-sky camera for passive visible observations of the full sky were installed. During PS106, OCEANET was complemented for the first time with a vertically-pointing motion-stabilized 35-GHz polarimetric Doppler cloud radar of type Mira-35 (Görsdorf et al., 2015) for continuous vertically resolved measurements of Doppler spectra produced by cloud vertical motions.

The Polly^{XT} system measures profiles of particle backscatter coefficient at three wavelengths (355, ~~512~~ 532 and 1064 nm), and of extinction coefficient as well as of the linear depolarization ratio at two wavelengths (355 and ~~512~~532 nm), respectively , details see Baars et al. (2016). Four near-field channels for detection of elastically and Raman-scattered light from nitrogen molecules are implemented at 355, 387, 532 and 607 nm to enable observations already at low heights starting at about 50 m above the instrument. An additional channel for detection of Raman-scattered light from water vapor at 407 nm allows

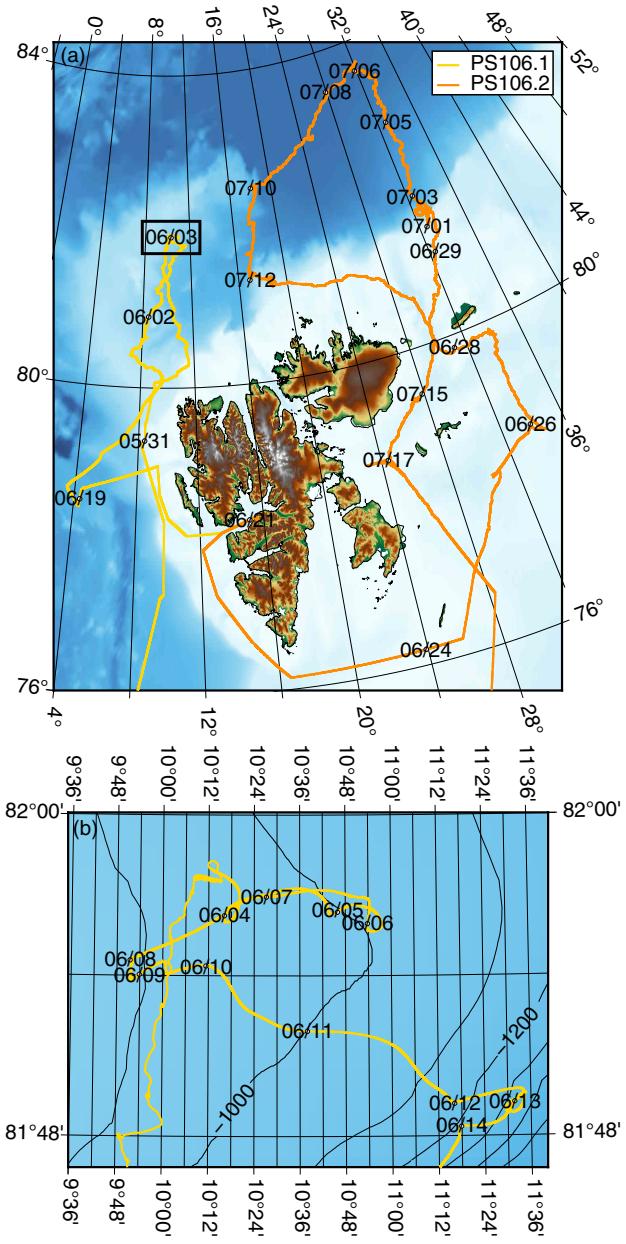

Figure 1. Track of RV Polarstern during PS106 (~~top~~a). PASCAL (PS106.1, yellow) was the first part of PS106 and was accompanied by a two-week drift (~~zoom of inlet in the bottom subfigure~~b) during which the ice floe camp was performed. Map ~~by Anna Nikolopoulos~~created with GMT (Wessel et al., 2019).

the retrieval of the water vapor mixing ratio (Dai et al., 2018) during low sunlight conditions. From the Polly^{XT} backscatter and extinction measurements, aerosol classification by their optical properties (Müller et al., 2007; Baars et al., 2017) up to

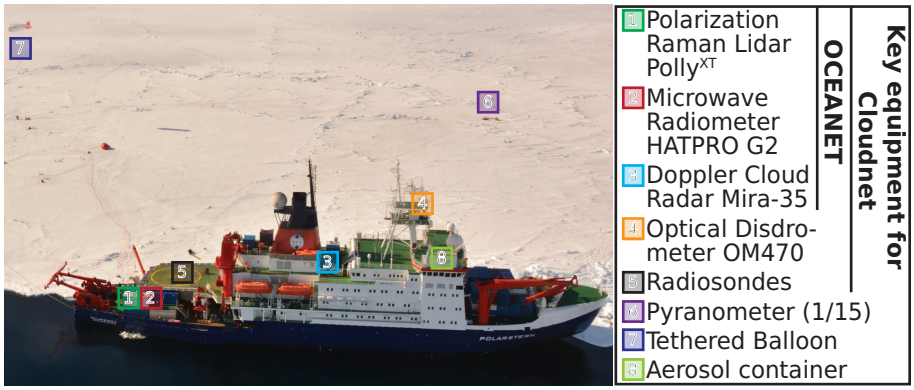

Figure 2. Polarstern during the ice floe camp performed during the PASCAL campaign. Annotated are the locations of some selected instruments for atmospheric measurements. (1–5) indicate the positions of the key instruments used for Cloudnet processing: Polly^{XT}, HATPRO, Mira-35, disdrometer and radiosondes. (6) denotes one of the 15 pyranometers comprising pyranometer network, at (7) was the tethered balloon launching site and at (8) aerosol in-situ measurements had been conducted. (1–3) are permanent part of OCEANET. Picture by N. Fuchs.

the retrieval of particle size distribution and number concentration (Müller et al., 1999; Baars et al., 2012) can potentially be derived. The polarization-sensitive detection channels allow to ~~determine the shape of the observed~~ distinguish between spherical and non-spherical aerosol and cloud particles (Kanitz et al., 2013a) and, for instance, to separate dust and non-dust particles in mixed aerosol layers (Baars et al., 2011). By applying the shape-detection capabilities of the polarization channels for the discrimination of spherical liquid droplets from non-spherical ice particles, heterogeneous ice formation in mixed-phase clouds can be studied (Seifert et al., 2015). Another application of depolarization observations in mixed-phase cloud studies is the estimation of cloud condensation nuclei (CCN) and ice nucleating particle (INP) concentrations (Mamouri and Ansmann, 2016). Due to the relatively short wavelengths of the lidar, e.g. compared to the cloud radar, it follows that the lidar is sensitive to rather small particles such as ~~aerosol~~ aerosols or small cloud droplets. Also attenuation, especially due to liquid clouds, has to be considered.

The MWR HATPRO provides estimates of the liquid water path (LWP), integrated water vapor (IWV), as well as humidity and temperature profiles with a temporal resolution of 1 Hz. The MWR measures the emission of radiation from the atmosphere in two frequency bands ranging from 22.24 – 31.4 GHz and from 51.0 – 58.0 GHz at 14 different channels. The MWR ~~datasets~~ data sets shown in this study are based on a retrieval that was created based on a long-term radiosonde ~~dataset from De Bilt, NL (52~~data set from Ny-Ålesund, Svalbard, Norway (78.9°~~06'~~ N, ~~5~~11.8°~~11'~~ E, ~~4~~11 m hasl, WMOCode 6260) according to Löhnert and Crewell (2003). ~~We are aware of possible differences that may arise by applying a mid-latitude retrieval to Arctic measurements but do think that the atmospheric conditions in summer in the Arctic are comparable to those in winter in the Netherlands. Nevertheless the preparation of an Arctic retrieval based on ERA-Interim data is in progress.~~

During PS106, the Ka-band Doppler radar Mira-35 was set-up to emit pulses with a width of 208 ns at a pulse repetition frequency of 5000 Hz. This corresponds to a vertical resolution of 31.18 m. The upper limit of the measurement range was set to 15 km. The Doppler spectrum was derived from the backscattered signals of 256 consecutive pulses. To allow the correction of the cloud radar data for the vessel movement, the whole spectrum (including noise) has been stored with a temporal resolution of 4 Hz and a Doppler resolution of 0.08 m s^{-1}. This correction has been done in a post processing procedure which is explained in Sect. 3.1. From the profiles of the Doppler spectra, the different Doppler moments such as radar reflectivity, Doppler velocity, and Doppler spectral width were determined as described in Görsdorf et al. (2015). The linear depolarization ratio (LDR) was obtained from the ratio of the radar reflectivity factor observed in the co- and cross-channels of Mira-35 and provides information about the hydrometeor shape (Bühl et al., 2016). In contrast to the lidar, the longer wavelength of operation of the cloud radar defines its sensitivity to range from cloud hydrometeors to slight precipitation. Especially in the case of shallow stratiform clouds, as they dominated the measurements during PS106, attenuation effects can be neglected. The OCEANET ~~datasets~~ data sets of HATPRO, Polly^{XT} and Mira-35 are publicly available through the Open Access library PANGAEA ~~(Griesche et al., 2019a, b, c)~~(Griesche et al., 2020b, c, 2019c).

2.2 Auxiliary instrumentation

Added value of the OCEANET measurements can be obtained when they are accompanied by additional observations. During the two-week ice floe camp performed in the frame of PASCAL, a tethered balloon site was set up for turbulence and radiation observations (Egerer et al., 2019) and a network covering 15 pyranometers to determine the spatial variability of the solar radiation was installed ~~(Barrientos Velasco et al., 2019)~~(Barrientos Velasco et al., 2020). In the context of this study, the turbulence as determined from the three-dimensional wind vector measured with high temporal resolution of several tens of Hertz by an ultrasonic anemometer attached to the tether of the balloon was used. To obtain mass and number concentration as well as optical properties and filter samples of the aerosol at the surface, a container equipped with instrumentation for aerosol in-situ measurements was installed on the deck of Polarstern and was measuring continuously during the whole two-month cruise (Kecorius et al., 2019). Also aboard Polarstern, measurements of the optical thickness of the cloud-free atmosphere were performed using a hand-held Solar Light Microtops Sun photometer. The Sun photometer measurements are already available through the ~~AErosol RObotic NETwork~~ **AE**rosol **RO**botic **NET**work (AERONET) project. An optical disdrometer, which is part of the OceanRAIN network (Klepp et al., 2018), mounted on the crows nest of the RV was continuously measuring the precipitation rate for different hydrometeor types and size bins. Additionally, launches of Vaisala RS92-SGP radiosondes (Jensen et al., 2016) were conducted every 6 hours (shortly before 5, 11, 17 and 23 UTC to reach 100 hPa approximately at 6, 12, 18 and 24 UTC) to obtain in-situ profiles of temperature (ΔT=0.5°C), relative humidity (ΔRH=5%), pressure (Δp=1 hPa), and horizontal wind speed (Δv=0.15 ms^{-1}) and direction (Δ°=2°).

Table 1. Overview of the ~~ship-borne~~instrumentation deployed during PS106 that had been used for processing of the Oceanet observations.

Instrument Type	Reference	Measured Quantities	ν: Frequency λ: Wavelength R: Range of Measurement P: Precision	Time Resolution
Raman Lidar				
Polly^{XT}	Engelmann et al. (2016)	Particle backscatter coefficient	$\lambda = 355, 532, 1064$ nm R: 0.1–15 km, 0–1 km^{-1} sr^{-1} P: 7.5 m; 1e-5 km^{-1} sr^{-1}	10 min -1 hour
		Particle extinction coefficient	$\lambda = 355, 532$ nm R: 0.3–5 km, 0–10 km^{-1} P: 300 m; 1e-2 km^{-1}	
		Particle linear depolarization ratio	$\lambda = 355, 532$ nm R: 0.1–15 km, 0–0.5; P: 7.5 m; 0.02	
Microwave Radiometer				
RPG HATPRO-G2 first generation dual profiler	Rose et al. (2005)	Integrated water vapor (IWV)	$\nu = 22.24$–31.4 GHz R: 0–35 kg m^{-2} P: 0.2 kg m^{-2}	1 Hz
		Liquid water path (LWP)	$\nu = 22.24$–31.4 GHz R: 0–1 kg m^{-2} P: 0.02 kg m^{-2}	
		Brightness temperature (TB)	$\nu = 51.0$–58.0 GHz R: 0–330 K P: 0.2–1 K	
Doppler Cloud Radar				
Metek Mira-35	Görsdorf et al. (2015)		$\nu = 35.5$ GHz	3.5 sec
		Radar reflectivity factor	R: 150–13000 m; -55–20 dBZ P: 3 m; 2 dBZ	
		Linear depolarization ratio	R: 150–13000 m; -26-0 dB P: 30 m; 1 dB	
		Hydrometeor vertical velocity	R: 150–13000 m; -11–11 m s^{-1} P: 30 m; 0.08 m s^{-1}	
Optical Disdrometer				
Eigenbrot ODM470	Klepp et al. (2018)	Particle size distribution	$\lambda = 880$ nm R: 0.04–22 mm P: 0.03–0.5 mm	1 min
Tethered balloon				
Ultrasonic anemometer	(Egerer et al., 2019)	3-D wind vector	R: 0–20 ms^{-1}	50 Hz
Metek uSonic-3 Class A		sonic (virutelle) temperature	R: -35–55°C	50 Hz
Pyranometer network				
15 Pyranometer EKO Instruments ML-020VM	(Barrientos Velasco et al., 2020)	Spectral irradiance	R: 0.3–1.1 μm	1 Hz
Sunphotometer				
Solar Light 540 Microtops II	(Porter et al., 2001)	Aerosol optical thickness	$\lambda = 340, 380, 440,$ $500, 675, 870, 936, 1020$ nm	On demand

3 Data processing and synergistic retrievals

Aim of the OCEANET observations from PS106 was to provide a continuous vertically-resolved view on cloud and aerosol macro- and microphysical properties in order to enhance the understanding of the Arctic atmosphere system and to support partner projects with ~~datasets~~ data sets for radiative transfer calculations and turbulence studies. To derive continuous products of cloud and aerosol properties, the shipborne OCEANET remote sensing observations were processed using the synergistic retrieval algorithm Cloudnet (Illingworth et al., 2007). In this section, we describe the extension of the standard Cloudnet algorithms by additional simple but operationally applicable products providing estimates of cloud droplet and ice crystal effective radius and the cloud-turbulence parameter eddy dissipation rate (EDR). The procedure for minimizing the influence of the RV motion on the measurement of vertical velocities with Mira-35, which are required for the EDR retrieval, is also explained below.

3.1 Correction of vertical-stare cloud radar observations for ship motion

A structural requirement to derive valid vertical velocity from a Doppler cloud radar is a vertical pointing radar without an own vertical-velocity component. When the cloud radar is pointing off-zenith, the measured vertical-stare Doppler velocity will be biased by an additional component introduced by the horizontal wind. Based on high resolved horizontal wind data and the radar beam incident angle, a correction is possible for this bias (Wulfmeyer and Janjić, 2005). For PS106, a different approach was chosen. Similar to the approach described by Achtert et al. (2015), the cloud radar was mounted on an active stabilization platform (Fig. 3 (~~b~~a)), which was in our case a predecessor of the SOMAG AG Jena – GSM 4000 (SOMAG, 2017). This platform actively leveled out the roll and pitch movement of the RV, ideally in a way that no correction of horizontal-wind effects was necessary. ~~On the other hand,~~

Figure 4 shows a comparison of the pitch and roll angle time series during ice breaking conditions from 1 June 2017 07:00 UTC – 3 June 2017 8:00 UTC measured by the vessel's own inertial measurement unit (IMU) and directly at the cloud radar. As the platform itself did not serve any position determination we made use of a single board computer (Beaglebone Blue) with integrated IMU. During the ice transit and the ice floe camp periods, the stabilization platform ensured an accuracy of the leveling of $\pm 0.5°$. The 2-sigma standard deviation during the ice transit (ice floe camp) was found to be $0.32°$ ($0.34°$), thus 95% of the datapoints show an accuracy of $89.68°$ ($89.66°$). During the open-sea passage of RV Polarstern, the accuracy of the stabilization was reduced to around $\pm 1°$ with a 2-sigma standard deviation of $0.7°$.

An additional bias of the true Doppler velocity can occur if the cloud radar itself moves ~~in a vertical direction, the resulting~~ vertically: the vertical velocity superimposes the measured Doppler velocity. In the case of a moving RV, the vertical movement is induced by the RVs heave rate and rotation. The necessary heave correction was done in a post-processing procedure which will now be introduced.

To enable the correction, the complete cloud radar Doppler spectra as well as the motion data (rotation and translation) of Polarstern were stored with a resolution of 4 Hz and 20 Hz, respectively, throughout the entire cruise. The heave rate of the

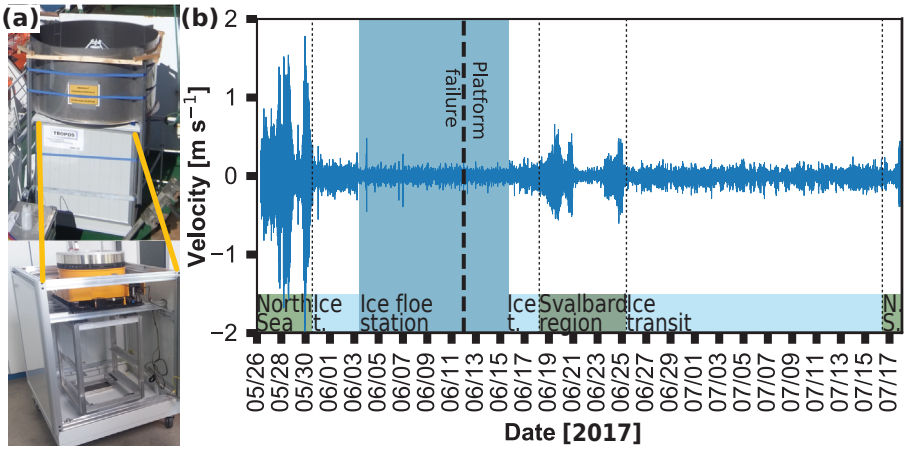

Figure 3. (a) The cloud radar aboard Polarstern and the stabilization platform. (b) shows the time series of the cloud radar heave rate during PS106. The thick dashed vertical line indicates the moment when the stabilization platform got a malfunction. At the bottom a rough localization of Polarstern is annotated (green: North Sea (N.S.), light blue: Ice transit (Ice t.), dark blue: Ice floe camp, dark green: Svalbard region).

cloud radar v_{C_z} was determined by summing up the z-component of the cross product between the rotation vector of Polarstern $\boldsymbol{v_{P_R}}$ and the position of the radar $\boldsymbol{X_R}$ relative to the mass centre of the RV

$$\boldsymbol{v_R} = \boldsymbol{v_{P_R}} \times \boldsymbol{X_R} = \begin{pmatrix} P_{pitch} \\ P_{roll} \\ P_{yaw} \end{pmatrix} \times \begin{pmatrix} x_R \\ y_R \\ z_R \end{pmatrix} = \begin{pmatrix} v_{R_x} \\ v_{R_y} \\ v_{R_z} \end{pmatrix} \tag{1}$$

with the z-component of the translation vector of Polarstern $v_{P_{T,z}}$

$$v_{C_z} = v_{R_z} + v_{P_{T,z}}. \tag{2}$$

In Figure 3 (b) the time series of v_{C_z} for PS106 is shown. The heave rate correction was done by shifting each individual Doppler spectrum opposite to the cloud radar heave rate. An illustration of this procedure is shown in Fig 5. In an initial step, the cross correlation between the timestamps of the two data sets, the cloud radar Doppler spectrum and the cloud radar heave rate, was calculated to check for a possible time shift between both ~~datasets~~data sets. This was found to be 0.25 s. Subsequently, the two values of v_{C_z} from before and after the current Doppler spectrum have been linearly interpolated onto its respective time. Finally, the spectrum was shifted according to the number of spectral bins determined by the Doppler resolution ($\Delta v_{DopplerSpectrum} = 0.08\,\mathrm{m\,s^{-1}}$) and the interpolated heave rate.

The effect of the heave correction is illustrated in ~~Figure~~Fig. 6. In Figure 6 (a) the uncorrected Doppler velocity measured on 30 May 2017 between 00:00 – 01:00 UTC, together with the respective histogram of the velocities is shown. The ~~RVs~~ RV's

~~(a) The cloud radar aboard Polarstern (a) and the stabilization platform (b). (c) shows the time series of the cloud radar heave rate during PS106, an overview of the respective area where Polarstern was located. The dashed vertical line indicates the moment when the stabilization platform got a malfunction. At the bottom a rough localization of Polarstern is annotated (green: North Sea (N.S.), light blue: Ice transit (Ice t.), dark blue: Ice floe camp, dark green: Svalbard region (Svalbard)).~~

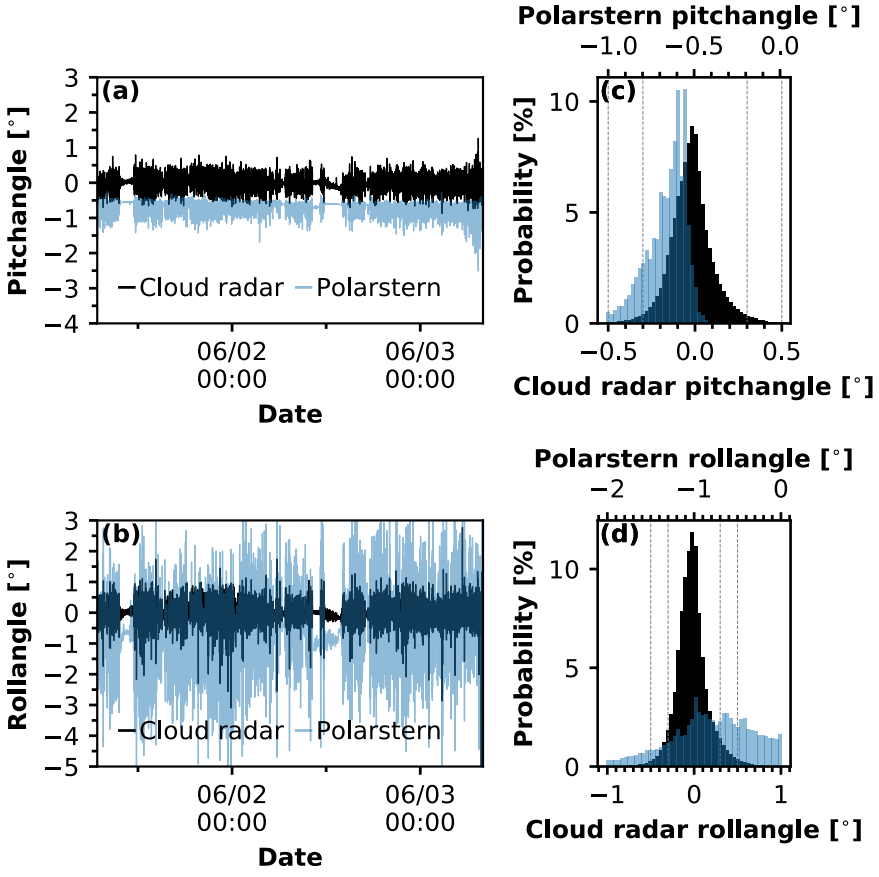

Figure 4. Pitch (a) and roll (c) of Polarstern (blue) and cloud radar (black) during the ice transit of Polarstern from 1 June 2017 07:00 UTC – 3 June 2017 8:00 UTC. In (b) and (d) the respective histogram is shown (note the different axes scale of the cloud radar data (bottom axis of each histogram) and Polarstern data (top axis)). The dashed lines indicate a rotation angle of ±0.5° and ±0.3°.

movement is visible in both, in the time-height cross-section of the Doppler velocity as stripes of enhanced or reduced velocity throughout the whole column as well as in the broadening of the histogram. The same is presented in Fig. 6 (b) but for the corrected Doppler velocity.

To evaluate the effect of the heave correction, we calculated the Fourier spectrum of the corrected and uncorrected Doppler velocity (Fig. 6 (e+f)). Continuous time series of 1 hour of Doppler velocity in the highest possible range gates of the cloud were analyzed. To quantify the impact of the heave correction the integral of the frequency range which was most affected

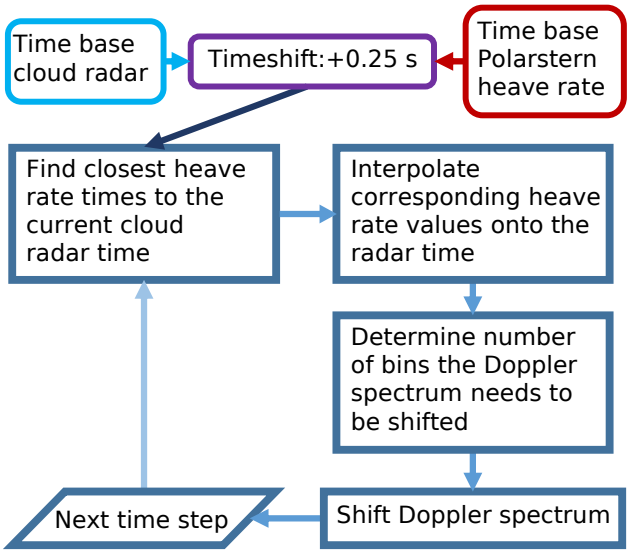

Figure 5. Flowchart of the heave rate correction.

by the ship's movement (0.1 – 2 Hz) was calculated both for the corrected and for the uncorrected data. The heave correction reduced the fraction of the ship's movement in the power spectral density of the cloud radar Doppler velocity by a factor of 15.

3.2 Retrieval of eddy dissipation rate

The rate at which turbulence kinetic energy is transferred from larger eddies into smaller ones and eventually dissolve into thermal energy is the EDR. This is used as a quantitative proxy of atmospheric turbulence. Several approaches to retrieve the EDR are common. Methods exist for in-situ measurements from aircraft- (Nicholls, 1978; Nucciarone and Young, 1991; Meischner et al., 2001), helicopter- (Siebert et al., 2006a), and balloon-borne (Caughey et al., 1979; Siebert et al., 2006b), as well as for meteorological tower instruments (Caughey et al., 1979; Kaimal et al., 1976; Zhou et al., 1985). Additional retrievals for remote sensing observation have been developed (Borque et al., 2016; Sathe and Mann, 2013). These methods are based on the Doppler velocity structure function derived from vertically-pointed Doppler lidar (Frehlich and Cornman, 2002) or Doppler radar (Lothon et al., 2005) or a combination of the width of the Doppler spectrum and the Doppler velocity measurements (Meischner et al., 2001). Other retrievals use time series analyses of vertical velocities from vertical-stare Doppler radar (Shupe et al., 2012; Kalesse and Kollias, 2013) or Doppler lidar observations (O'Connor et al., 2010).

Typical values for EDR in clouds spread between $10^{-1} - 10^{-8}\,\mathrm{m^2\,s^{-3}}$. Borque et al. (2016) report EDR of maritime and continental stratiform clouds in the order of $10^{-4} - 10^{-2}\,\mathrm{m^2\,s^{-3}}$ and $10^{-7} - 10^{-2}\,\mathrm{m^2\,s^{-3}}$, respectively. In cumulus clouds with weak updrafts, EDR had been found in a range between $5 \cdot 10^{-5} - 10^{-2}\,\mathrm{m^2\,s^{-3}}$, whereas values up to $10^{-1}\,\mathrm{m^2\,s^{-3}}$ were found for cumulus clouds with strong updrafts (Siebert et al., 2006a). In cumulonimbus clouds, Meischner et al. (2001) found values

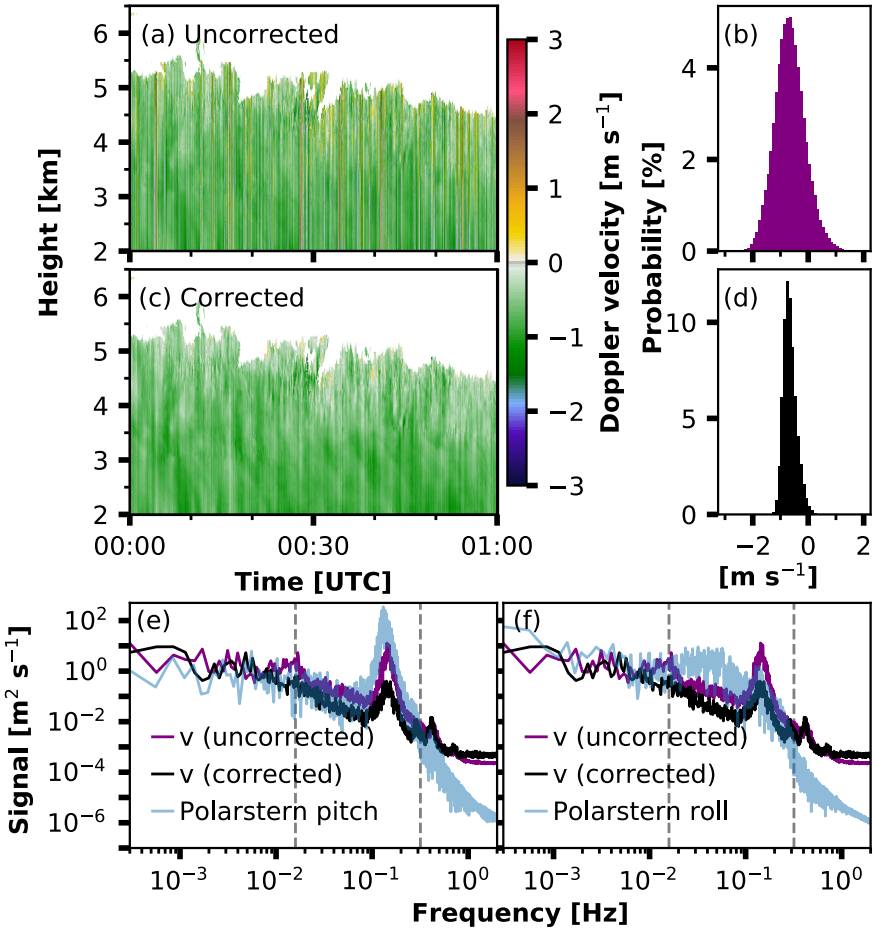

Figure 6. Uncorrected (a) and corrected (c) Doppler velocity during PASCAL on 30 May 2017 between 00:00 – 01:00 UTC. ~~In the small box in the upper right corner the respective histogram of the presented Doppler velocity is shown.~~ (b) and (d) represent the respective histogram of the presented Doppler velocity . Negative values denote downward motion. In (e) and (f) the mean Fourier spectrum of the uppermost, continuous time series of the (uncorrected) Doppler velocity during the same period in black (purple) is shown. In (e) in addition the spectrum of the Polarstern pitch movement during this period is depicted. In (f) the respective spectrum of the roll movement is shown. The dashed lines in (e) and (f) indicate the frequency range which was used to quantify the effect of the heave correction.

for EDR between $10^{-6} - 5 \cdot 10^{-2}$ m^2 s^{-3}. For low clouds or fog at Chilbolton, UK, O'Connor et al. (2010) estimated the EDR to be in the order of $10^{-4} - 5 \cdot 10^{-2}$ m^2 s^{-3}.

The presented range of EDR for different cloud conditions suggests that also Arctic clouds might show characteristic differences for varying atmospheric conditions. The vertical alignment of the cloud radar during PS106 enables the determination of EDR from the vertical air motions observed in cloud layers. Below, we thus present a retrieval technique for EDR that can be applied to the OCEANET data set.

3.2.1 EDR from vertical-stare Doppler velocity power spectra

Assuming the turbulent energy dissipation is a homogeneous and isotropic process, the turbulent energy spectrum $S(k)$ within its inertial subrange is represented according to Borque et al. (2016) by

$$S(k) = A\varepsilon^{2/3}k^{-5/3}, \tag{3}$$

with $A = 0.5$ the Kolmogorov constant for a 1-D wind spectra (Sreenivasan, 1995). k represents the wavenumber, which is related to a length scale L ($k = 2\pi/L$) as well as to frequency f with $k = f/V_h$ and V_h as the horizontal wind speed and assuming a linear wind field. If in a log-log plot the observed spectra within the inertial subrange follows a $-5/3$ slope, ε can be estimated by

$$\varepsilon = \left(\frac{10^{k_0}}{A}\right)^{3/2} \tag{4}$$

where k_0 is the corresponding intercept of the linearized fit.

For this study, power spectra of the Doppler velocity with 4 Hz of continuous time series covering 5 minutes were calculated. To get the best estimate of the respective inertial subrange, the fit was determined by calculating a linear least-squares regression of the spectrum in 34 different wavenumber intervals. The corresponding wavenumber intervals Δk_i are depicted in Fig. 7 (a) together with the spectrum of the ~~verrtical~~ vertical velocity observed on 7 June 2017, from 10:28 - 10:43 UTC. Following Borque et al. (2016), a good fit was defined with a slope from the linear regression of -5/3 $\pm$ 20% (-5/3 $\pm$ 1/3). If this criteria was matched within more than one wavenumber interval the mean of all ε_i for one spectrum was calculated. In order to evaluate the EDR estimated by cloud radar measurements, it was compared to EDR derived from the tethered balloon (Egerer et al., 2019). The time periods used for deriving EDR from the tethered balloon was 15 minutes, during which it was located at a constant height above ground. ~~Two~~ As a measure to quantify the uncertainties of the two retrievals the standard deviation σ of all good fits was calculated.

Three comparisons had been done ~~, one~~ for situations where the tethered balloon was parked at a constant height within a cloud. One on 7 June 2017, with the tethered balloon being at 380 m height between 10:28 and 10:43 UTC~~and one on 9 June 2017, between 09:00 and 09:15 UTC.~~

. In Figure 7 (a) an intercomparison of the power spectrum derived by the tethered balloon measurements (red) with the spectrum ~~as it was~~ derived from the cloud radar Doppler velocity (blue) according to the techniques described above is shown for ~~the periodon 7~~this period. The other two comparisons were done on 5 June ~~2017. The~~ 2017, between 13:50 and 14:05 UTC at 330 m height and on 9 June 2017 09:00 – 09:15 UTC at 500 m height. The EDR values for these cases from the tethered balloon measurements were $8.90 \cdot 10^{-5} \pm 1.07 \cdot 10^{-5}\,\mathrm{m^2 s^{-3}}$ and $6.39 \cdot 10^{-5} \pm 5.48 \cdot 10^{-6}\,\mathrm{m^2 s^{-3}}$ while the cloud radar measurements gave $5.98 \cdot 10^{-5} \pm 3.53 \cdot 10^{-5}\,\mathrm{m^2 s^{-3}}$ and $2.26 \cdot 10^{-5} \pm 1.64 \cdot 10^{-5}\,\mathrm{m^2 s^{-3}}$, respectively.

The comparisons of the two retrievals showed that the values differ by a factor of 2–3. ~~For 7 June, the cloud radar retrieval underestimated the balloon value (Fig. 7 (a)) and vice versa for 9 June (not shown here).~~ This discrepancy is in the order of

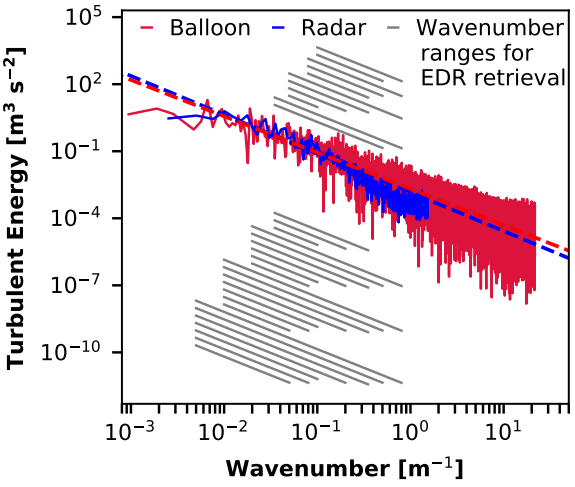

Figure 7. Fourier spectrum derived from cloud radar Doppler velocities (blue) and from tethered balloon (red) turbulence measurements on 7 June 2017 between 1027–1043 UTC at 380 m height with their respective averaged linearized fit depicted by the dashed line. The EDR values of the two methods were: $\varepsilon_{TetheredBalloon} = 2.65 \cdot 10^{-4}\,\mathrm{m^2 s^{-3}}$ and $\varepsilon_{CloudRadar} = 6.84 \cdot 10^{-4}\,\mathrm{m^2 s^{-3}}$ with standard deviation $\sigma_{TetheredBalloon} = 3.59 \cdot 10^{-5}\,\mathrm{m^2 s^{-3}}$and $\sigma_{CloudRadar} = 7.61 \cdot 10^{-4}\,\mathrm{m^2 s^{-3}}$. Grey lines: Illustration of the wavenumber intervals that had been used to check for a -5/3 slope of the Fourier spectrum.

magnitude as one could expect due to the spatial distance between the two measurements alone (about 200 m). The dashed line in Fig. 7 (a) is an example for the -5/3 slope and the black lines indicate the wavenumber intervals that had been used to check for a -5/3 slope of the Fourier spectrum.

~~Figure 7 (b) displays the time-height cross sections of EDR on 7 June 2017 between 100 – 800 m height. Until 12:00 the EDR was rather high with values up to $10^{-3}\,\mathrm{m^2 s^{-3}}$. After that, the EDR decreased rapidly down to values below $10^{-4}\,\mathrm{m^2 s^{-3}}$ and eventually the cloud dissolved.~~

3.3 Cloud macro- and microphysical properties from instrument Synergies

To acquire a data set suitable for the statistical evaluation of the macro- and microphysical properties of clouds observed during PS106, the instrument synergistic approach Cloudnet (Illingworth et al., 2007) was applied. This data set in addition serves to realize model evaluations (Illingworth et al., 2007) and radiative transfer calculations, e.g, with the Rapid Radiative Transfer Model for climate and weather models (RRTMG; ~~Iacono et al. (2008)~~Mlawer et al. (1997); Barker et al. (2003); Clough et al. (2005)). RRTMG is currently utilized for single column radiative transfer calculations. The model considers vertical profiles of relative humidity and temperature, standard atmospheric constituent profiles based on Anderson et al. (1986) and cloud macro and microphysical properties of clouds. These assignments include sets of effective radius and mass concentration of liquid and ice hydrometeors. In the following, the approaches for achieving these ~~dataset~~ data set requirements based on the PS106 remote-sensing observations are described.

3.3.1 Cloudnet

The instrument synergy approach Cloudnet (Illingworth et al., 2007) ~~,~~ which combines the observations from lidar, cloud radar, microwave radiometer, disdrometer and radiosondes was used to determine cloud physical properties during PS106. To illustrate this procedure, the Cloudnet approach will now be briefly introduced. The measurements are first averaged on a common grid with a vertical and temporal resolution of 31.18 m (resulting from the cloud radar resolution) and 30 s~~,~~ ~~respectively.~~ . To estimate the temperature at the respective time-height pixel, radiosonde-based profiles of thermodynamic variables are interpolated on the Cloudnet grid. If no radiosonde was launched from the RV but Polarstern was in the vicinity of Svalbard, soundings from Ny Ålesund (Maturilli, 2017) were substitutionally utilized. As a last fall-back option, data from the Global Data Assimilation System model (GDAS) with a horizontal and vertical resolution of 1° and 3 h (GDAS1) was used as meteorological input into Cloudnet.

Based on the observations scaled on the Cloudnet grid ~~, a classification~~ a categorization bit mask is derived, which assigns a series of 7 distinct features to the observed targets: clear yes/no; liquid yes/no; falling yes/no; wet bulb temperature below 0 °C yes/no; melting layer yes/no; aerosol yes/no; insects yes/no. The bitwise ~~classification~~ categorization ensures that each data point is characterized by a defined combination of these features. The detailed definition of the respective categorization bits is beyond the scope of this paper and has already been given by Hogan and O'Connor (2004).

Based on the individual combination of the ~~classification bits, a set of typical atmospheric targets is derived , as described by Hogan and O'Connor (2004).~~

~~Cloud droplets are assumed to be spherical and to have a large effective surface compared to ice crystals as they are in fact rather small but appear in high number. Their presence is determined by lidar measurements due to its sensitivity to small-sized but numerous particles. Hence a Cloudnet pixel with high backscatter and a distinct decrease after the signal is defined as liquid. The presence of ice is determined by a radar pixel indicating a falling particle at a dew point temperature $T < 0$ °C. If both criteria for liquid and ice, high lidar backscatter, and downward-pointing cloud radar vertical velocity are fulfilled at $T < 0$ °C the pixel is identified as mixed-phase. Besides using the air temperature, the melting layer is also identified by a cloud radar linear depolarization ratio LDR > -15 dB or a strong increase of the vertical velocity observed by the cloud radar. To estimate the temperature at the respective time-height pixel, radiosonde-based profiles of thermodynamic variables are interpolated on the Cloudnet grid. If no radiosonde was launched from the RV but Polarstern was in the vicinity of Svalbard, soundings from Ny Ålesund (Maturilli, 2017) were substitutionally utilised. As a last fall-back option, data from the Global Data Assimilation System model (GDAS) with a horizontal and vertical resolution of 1° and 3 h (GDAS1) was used as meteorological input into Cloudnet. Due to their rather small size but heterogeneous shape, aerosols are characterized by absence of a radar signal and low lidar backscatter signals which can show both strong or weak depolarization, depending on the aerosol type (Baars et al., 2017)~~categorization bits, an atmospheric target classification is derived as follows: 'Clear sky' is defined as no bit is set for the respective pixel. 'Cloud droplets only' are identified by only the droplet bit being set. The falling bit alone identifies 'Drizzle or rain'. Droplet and falling bit together are interpreted as 'Drizzle/rain & cloud droplets', falling and cold bit together as 'Ice'. Droplet, falling and cold bit combined give 'Ice & supercooled droplets'. The melting bit

being set alone identifies 'Melting Ice', and together with the droplet bit the pixel is defined as 'Melting ice & cloud droplets'. The aerosol and insects bit then are accordingly interpreted as 'Aerosol', 'Insects' or 'Aerosol & insects'. Following previous studies (e.g. Shupe, 2011; Mioche et al., 2015) we have defined mixed-phase clouds when (supercooled) liquid water and ice particles are detected in the same data point and when an ice cloud was observed with a liquid or mixed-phase cloud top layer.

Besides the phase of the cloud, the respective mass concentrations of ice and liquid water are determined were applicable. The liquid water content (LWC) is derived by scaling the MWR liquid water path adiabatically onto the cloud pixels defined as liquid or mixed-phase (Frisch et al., 1998; Merk et al., 2016). For pure-liquid data points, the approach of Frisch et al. (2002) is used to derive the cloud droplet effective radius from the observed radar reflectivity factor and liquid water path and an assumed width of the log-normal cloud droplet size distribution (which was, according to Miles et al. (2000), set to 0.35 in our study). The ice water content (IWC) is calculated using an empirical formula from Hogan et al. (2006) relating cloud radar reflectivity Z and temperature T. This approach for IWC is only applied for ~~those~~ clouds Cloudnet classified as ~~ice clouds~~'Ice' or 'Ice & supercooled droplets'. In this step also a correction for potential attenuation of the cloud radar signal due to the presence of liquid water is made~~. Dealing with thin Arctic clouds, this was no big issue for this study~~.

3.3.2 Ice crystal effective radius

As discussed above, Cloudnet offers a variety of retrievals for ice microphysical parameters. Nevertheless, the continuous application of radiative transfer calculations requires a consistent availability of ice and liquid hydrometeor effective radius and mass concentration. While Cloudnet already contains retrievals for effective radius and mass concentration of liquid droplets, as well for ice water content, so far no operational retrieval for ice effective radius is available. We therefore decided for the implementation of a new approach which is based on the combination of a definition of the effective radius as the ratio of the third to the second moment of the particle size distribution (PSD) and an empirical relationship between the visible extinction coefficient α, cloud radar reflectivity Z, and model temperature T. Similar as for IWC (and α), $r_{e_{ice}}$ is only calculated for datapoints where Cloudnet classified ~~ice clouds~~'Ice' or 'Ice & supercooled droplets'.

Using the ratio of the second to the third moment of the PSD, the effective radius $r_{e_{ice}}$ can be related to IWC and α (Delanoë et al., 2007). This yields for $r_{e_{ice}}$:

$$r_{e_{ice}} = \frac{3}{2}\frac{IWC}{\rho_i \alpha} \cdot 10^6 \ (\mu\text{m}), \tag{5}$$

with ρ_i as density of the solid ice ($\rho_i = 917\,\text{kg}\,\text{m}^{-3}$). Both, IWC and α have been calculated using empirical relationships between IWC or α, and the cloud radar reflectivity Z of a 35-GHz cloud radar and temperature T (Hogan et al., 2006).

Finally, we found for the ice crystal effective radius a ~~Z-T~~ $Z - T$ relationship:

$$r_{e_{ice}} = \frac{3}{2\rho_i} 10^{C_{ZT} \cdot ZT + C_Z \cdot Z + C_T \cdot T + C} \cdot 10^6 \ (\mu\text{m}), \tag{6}$$

with $C_{ZT} = -2.05 \cdot 10^{-4}$, $C_Z = 1.6 \cdot 10^{-3}$, $C_T = -1.71 \cdot 10^{-2}$ and $C = -1.52$.

To estimate the error of the identified effective radii of the ice crystals, an error propagation of Eq. (6) had be done using the respective error for IWC and α from Hogan et al. (2006).

3.3.3 ~~Fog detection~~Detection of low-level stratus clouds

During PS106, frequently low-level stratus clouds (cloud base < 165 m) ~~or fog~~ have been observed. These situations were often associated with ~~an~~ a strong attenuation of the lidar beam within the lowest few hundred meters above Polarstern due to the high optical thickness of these clouds. The cloud radar, in turn, has its technical limitation in detecting the lowest part of the boundary layer ~~. The measurements of Mira-35 start in a height of~~ below 155 m ~~above the instrument~~range (165 m above sea level). Due to the instrument synergy approach of Cloudnet this is also the height of the lowest Cloudnet data pixel. Thus, the low-level clouds which occurred during PS106 introduced on the one hand issues to the Cloudnet retrieval due to misinterpretation of attenuated lidar signal as missing signal. On the other hand, since most current statistics of Arctic clouds do not consider clouds in such a low altitude, these clouds tend to be underrepresented in Arctic cloud statistics. To address these issues, we introduce a new Cloudnet classification category called ~~fog. Fog was~~ low-level stratus cloud. These clouds were identified by the Polly^{XT} signal-to-noise ratio (SNR, (Heese et al., 2010)) in the lowest 165 m above sea level. ~~If the SNR exceeded a value of 40 this was assumed to be due to the presence of fog~~The near-range channels of the Polly^{XT} system have a complete overlap already at 120 m above the instrument (Engelmann et al., 2016) and thus are suitable for the detection of clouds already well below the lowest cloud radar observation height, even though quantitative parameters such as (attenuated) backscatter coefficient from a single elastic backscatter signal cannot yet be determined at these heights.

From visual inspection of the Cloudnet data set we defined low-level stratus where the SNR exceeded the threshold value of 40. This value was obtained by evaluating signatures of attenuation in the time series of the Cloudnet attenuated backscatter coefficient, increased values of LWP time series, and correlation with the visibility sensor of Polarstern. Since the SNR is not yet range-corrected, this threshold-crossing at these low altitudes is very likely only due to the occurrence of ~~fog or~~ low-level clouds. The low level stratus base and top have been derived by simply using the lowest and highest range gate from Polly^{XT} where the SNR exceeded the threshold.

3.4 Retrieval of CCN- and INP number concentrations

Arctic clouds and their susceptibility to the presence of aerosol are still in focus of research ~~(Morrison et al., 2012)~~(Morrison et al., 2012) . Based on the measurements of Polly^{XT}, an estimation of cloud condensation nuclei (CCN) and ice nucleating particle (INP) properties is possible (Mamouri and Ansmann, 2016). To do so, profiles of the aerosol backscatter coefficient and depolarization ratio need to be determined. In a second step, these profiles are converted into profiles of the particle extinction coefficient using an appropriate lidar ratio (extinction-to-backscatter ratio).

The CCN number concentration (CCNC) and INP number concentration (INPC) profiles were estimated from profiles of the lidar-derived particle extinction coefficient at 532 nm by means of conversion parameters and published INP parameterization schemes (DeMott et al., 2010) as described by Mamouri and Ansmann (2016). The required conversion parameters for Arctic AERONET stations were determined in the same way as outlined by Mamouri and Ansmann (2016). We used multi-year

(2004-2017) Sun-photometer observations of the AERONET stations Thule, PEARL, Kangerlussuaq, Ittoqqortoormiit, and Hornsund to obtain the set of Arctic conversion parameters. These AERONET observations were made during the summer half years.

The direct retrieval of the CCN conversion parameters from the AERONET data (level 2, version 3, inversion products) revealed $C_1 = 18.6\,cm^{-3}$ and exponent $d_1 = 0.83$ for the range of extinction coefficients from 15 – 300 Mm^{-1} (500 nm AOD from 0.015 – 0.3 were measured). During the PS106 observations, the aerosol extinction coefficient was mostly around 1–10 Mm^{-1} in the lower part of the troposphere. The AERONET data for this low range of extinction coefficients indicates that conversion parameters of $C_2 = 10\,cm^{-3}$, $d_2 = 0.9$, $C_3 = 3.0\,cm^{-3}$, $d_3 = 1$ would be appropriate. The aerosol in the Arctic is fine-mode dominated and shows Ångstrom exponents (440–870 nm) typically between 0.9 and 1.8 (with an average of 1.5–1.6).

3.5 ~~Back trajectory analysis: Trace~~

~~To analyse the origin of an observed air mass and to classify the most likely continental source region, the trajectory analysis tool Trace based on HYSPLIT (Stein et al., 2015) and GDAS1 data as dynamic driver were used. This trajectory analysis tool calculates 10-day backward trajectories of an 27-member trajectory ensemble. To estimate the most likely source region of the trajectory, the residence time below the mixing depth provided by the GDAS1 data set was used and categorized in different land cover categories (Foth et al., 2019; Radenz and Seifert, 2019).~~

4 Results

4.1 Case studies

Based on near-surface and radiosondes measurements, model data and satellite observations Knudsen et al. (2018) gave a detailed description of the synoptic situation during the PASCAL campaign. They defined three periods (cold, warm and normal period). Three case studies will be presented in the following ~~. They were, on the one hand,~~ which are all within the warm period (WP 30 May – 12 June 2017). These two weeks of the WP are characterized by warm and moist air advection from the south crossing Norway and Greenland (Fig. 8).

The three cases between 7 June and 9 June 2017 were chosen to demonstrate the potential OCEANET offers~~, by presenting the~~ . Within these three days the near-surface temperature first dropped from -3.5°C on 7 June 2017 00:00 UTC to -7.5 °C on 8 June 2017 05:00 UTC with an ensuing increase to 1.0°C on 9 June 2017 22:00 UTC due to warm air advection. These cases were, on the one hand, selected to represent the capabilities of the standard Cloudnet products and of Polly^{XT} ~~. On~~ and on the other hand ~~, these cases are selected~~ to illustrate the new products introduced in this study.

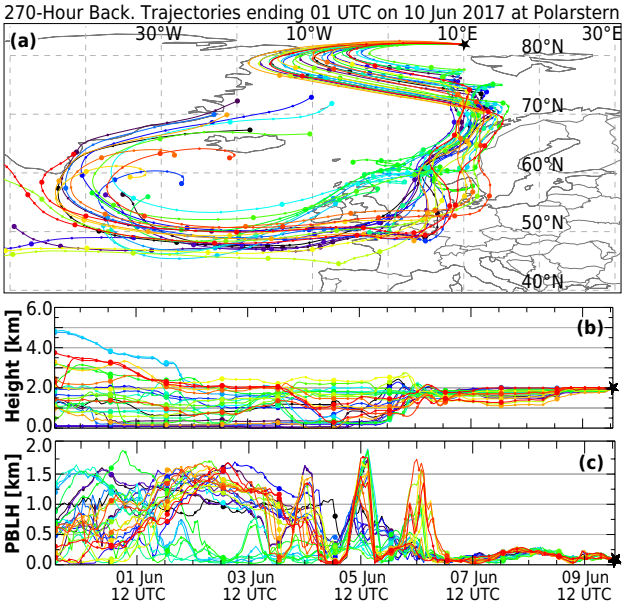

Figure 8. (a): Ensemble of 27 10-day back-trajectories arriving at the position of Polarstern at 01 UTC on 10 June 2017 in 2000 m height. (b) shows the height of the trajectory and (c) the respective planetary boundary layer height (PBLH).

4.1.1 Precipitating layered cloud: 9 June 2017, 00:00 – 18:00 UTC, ice floe camp

An overview of the capability of the OCEANET measurements and its application to analyze cloud and aerosol structures and their interactions will be presented for a complex case that occurred over Polarstern on 9 June 2017 between 00:00 – 18:00 UTC. The radiosonde profiles for this period are shown in Fig. 9 up to a height of ~~2000~~2500 m. The observations of the cloud radar, the lidar and the MWR are depicted in Fig. 10.

The presented day reveals a rather complex situation. Starting at 00:00 UTC, Cloudnet classified a liquid stratocumulus layer between 600 – 900 m height with a cloud top temperature of -1.5 °C. This layer slowly descended, reaching a cloud base of about 400 m and cloud top of about 800 m at 05:00 UTC. The LWP during this period was rather constant with a mean value of 50 g m^{-2} with two distinct peaks: one at around 01:50 UTC and the other one around ~~04~~03:45 UTC with a LWP of up to 70 g m^{-2}, both associated with a slight increase in cloud depth. The constantly high values of EDR until roughly 05:00 UTC (~~10^{-4} – 10^{-3}~~10^{-4} – 10^{-3} m^{2}s^{-3}, Fig. 11 (d)) indicate strong turbulent mixing of the cloud layer.

At around 05:30 UTC, a transformation of the cloud occurred~~, the~~ . The LWP increased up to 160 g m^{-2} and precipitation started, almost reaching the ground (the disdrometer aboard Polarstern showed no precipitation signal, not shown here). Though the LDR showed no increased values, the presence of ice was identified due to detection of enhanced radar reflectivity and vertical velocity and thus a mixed-phase cloud was classified between 05:30 – 06:30 UTC. During this period, the retrievals of the ice and liquid hydrometeor size as proposed in this paper may be influenced by each other. Both retrievals are based on the same quantity, the radar reflectivity, which is characterized by the largest peak in the Doppler spectrum. To tackle this issue, a

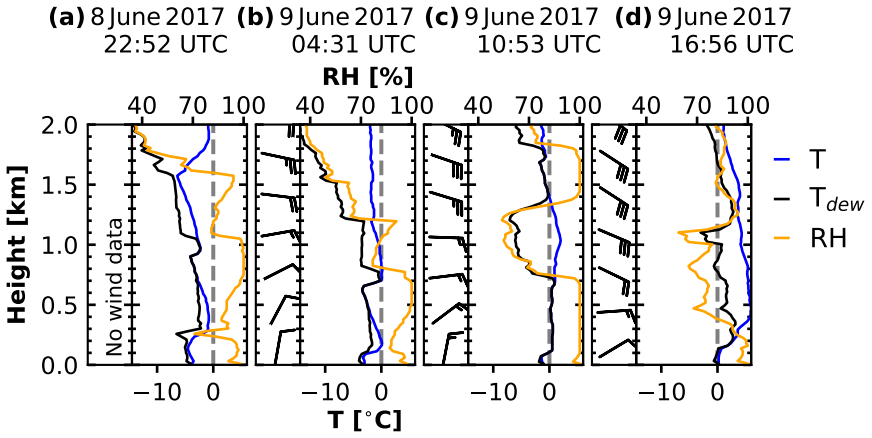

Figure 9. Thermodynamic profiles from radiosondes launched aboard Polarstern on (a) 8 June 2017 at 22:52 UTC, (b) 9 June 2017, 04:31 UTC, (c) 9 June 2017, 10:53 UTC, and (d) 9 June 2017,16:56 UTC up to 2 km height. Each sounding is divided into two parts: left side the wind barbs, right side the temperature (blue), dew point temperature (black), and relative humidity (orange) profiles.

peak separation of the Doppler spectrum as it is proposed e.g., by Shupe et al. (2004), Kalesse et al. (2016b) or Radenz et al. (2019) would be necessary. This would offer the opportunity to calculate the effective radius of the different hydrometeors species based on their particular reflectivity but is beyond the scope of this paper. At around 06:30 UTC the interpolated temperature of the surrounding radiosonde profiles reached 0 °C leading to an immediate transition from a mixed-phase to a pure liquid cloud. Therefore, no IWC and no ice effective radius were determined under these conditions.

A second transition of the cloud situation during this day is associated with an altocumulus layer which was located above the stratocumulus. Around 09:00 UTC this mid-level cloud layer with a cloud-top temperature of -1°C occurred at 1900 m height over Polarstern. As this layer increased in geometrical and optical depth, shading effects reduced the cloud-top radiative cooling of the cloud below as already observed in (Shupe et al., 2013). This led to a collapse of the EDR in the lower layer at around 12:00 UTC (Fig. 11 (d)) and finally to a dissipation of the cloud. The values for ε in the altocumulus were about the same order of magnitude as for the stratocumulus, indicating that the upper cloud was able to effectively cool to space. Starting at about 14:00 UTC the altocumulus formed a two-layer structure at 1500 m and 1200 m, respectively. Due to the shading of the upper layer, the lower one lost its turbulent moment and the cloud dissipated shortly after. The altocumulus was classified as pure ice cloud, probably due to the fact that the lidar signal was already fully attenuated in the lower layer which impedes the classification as liquid at an ambient temperature below 0°C. At around 11:00 UTC, the temperature exceeded 0°C, due to which Cloudnet changed its classification from an ice cloud to a liquid cloud. After persisting for about 4 hours with ~~very~~ rather low EDR, the stratocumulus started to dissipate at around 16:00 UTC. This offered the lidar the opportunity to observe the aerosol structure above Polarstern in the subsequent hours (Fig. 12 (b)).

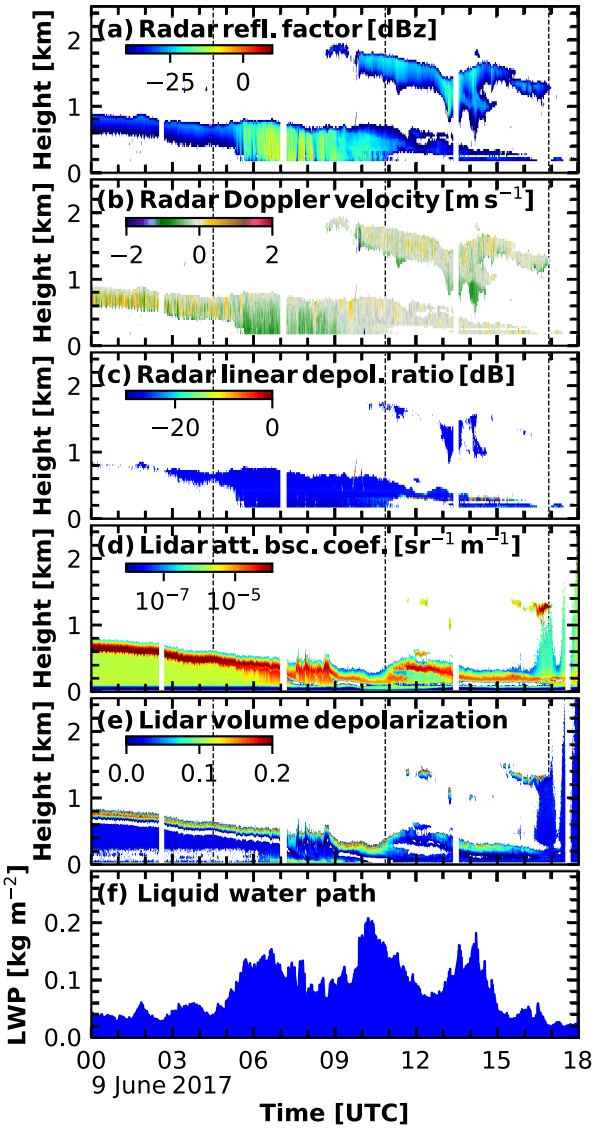

Figure 10. OCEANET observations on 9 June 2017 between 00:00 – 18:00 UTC. (a), (b) and (c) show the radar reflectivity factor, Doppler velocity, and linear depolarization ratio ~~, respectively~~. (d) and (e) depict the lidar attenuated backscatter coefficient at 1064 nm and volume depolarization ratio at 532 nm~~, respectively~~. In (f) the liquid water path derived by the microwave radiometer is shown. The dashed vertical lines mark the time of the radiosonde launches on 9 June 2017 (note: the time of the first launch shown in Fig. 9 was before the plotted profiles of the measurements start).

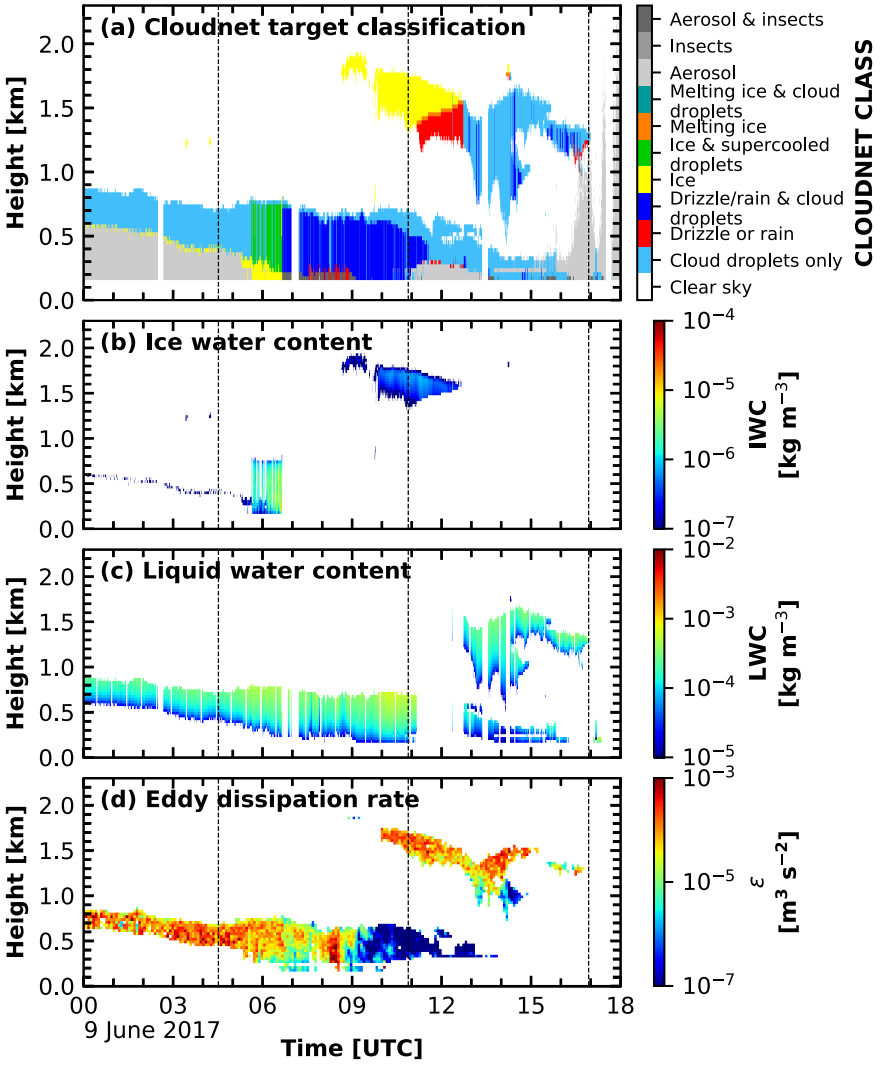

Figure 11. (a) Cloudnet target classification, (b) ice water content, and (c) liquid water content for 9 June 2017 between 00:00 – 18:00 UTC. (d) shows the time-height profile of EDR calculated from the cloud radar Doppler velocity. The dashed lines mark the time of the radiosonde launches as shown in Fig. 9.

4.2 ~~Aerosol case: 9 June 18:00 UTC – 10 June 2017 11:00 UTC, ice floe camp~~

4.1.1 Aerosol case: 9 June 18:00 UTC – 10 June 2017 11:00 UTC, ice floe camp

Between 9 June 18:00 UTC – 10 June 2017 11:00 UTC, one of the rare cloud-free events of PS106 occurred and Polly^{XT} observed aerosol layers in the free troposphere (Fig. 12 (d)). The respective radiosonde profiles for this period are shown in Fig. 12 (a–c). Based on a ~~Trace airmass source~~ trajectory analysis of 27 10-day HYSPLIT back-trajectories (Stein et al., 2015), a southern inflow for air masses above the boundary layer is identified for this period. At the 2000 m height level, the trajectories show that these were long-range-transported aerosol layers that originated over continental Europe (Fig. 8) with a high chance of being within the planetary boundary layer at that time. Below 2000 m height, the trajectories indicate that pathways mainly crossed the north sea and the Atlantic ocean (not shown).

The 1064-nm lidar attenuated backscatter coefficient and the 532-nm volume depolarization ratio are shown in Fig. 12 (d, e). These measurements reveal the existence of three aerosol layers being present over Polarstern on 9 June 2017 around 18:00 UTC. A shallow layer at 500 m height staying roughly at the same altitude as long it was observed by Polly^{XT}. A second one is visible between 1000 and 1500 m height ascending to 2500 m at 00:00 UTC on 10 June 2017. At 07:00 UTC on 10 June 2017, a liquid cloud formed at the top of this layer. A third aerosol layer with a liquid cloud embedded at 2300 m height, being rather constant in altitude, was present between 19:00 – 21:00 UTC on 9 June 2017.

In Figure ~~(13)~~13, a detailed analysis of the aerosol optical properties as derived from the lidar measurements from the time period of 00:00 – 02:20 UTC is presented. During this period, two layers were detected and are visible in the profiles of the backscatter coefficient at all three wavelengths (Fig. 13 (a)). The rather strong wavelength dependence of the backscatter coefficient, as shown by the high Ångstrom exponents (Fig. 13 (b)) in both layers, indicates the presence of small aerosol particles. A back-trajectory analysis and the values for the Ångstrom exponent indicates that air masses transporting polluted aerosol from continental Europe are most probably the source for the upper aerosol layer. The lower aerosol layer on the other hand is most-likely a mixture of down-mixed continental and upward-mixed marine aerosol.

Based on the aerosol optical properties retrieved by Polly^{XT} an estimation of the CCNC was done for all three combinations of conversion factor and extinction exponent as mentioned in Sect. 3.4. We chose the second combination (C_2 = 10 cm^{-3} and d_2 = 0.9) to illustrate the results in Fig. 13 (d). The mean values of CCNC for the upper aerosol layer in this case was found to be $\bar{n}_{CCN,2}$ = 180 cm^{-3}. For the two other combinations, we found $\bar{n}_{CCN,1}$ = 260 cm^{-3} and $\bar{n}_{CCN,3}$ = 75 cm^{-3}, respectively. For the lower aerosol layer, we found $\bar{n}_{CCN,2}$ = 70 cm^{-3}. For the two other combinations, we found $\bar{n}_{CCN,1}$ = 110 cm^{-3} and $\bar{n}_{CCN,3}$ = 25 cm^{-3}, respectively. The uncertainty of this method is up to 200% (dashed lines in Fig. 13 (d)). In addition, the INPC was calculated for a fixed temperature of -15°C. The results are shown in Fig. 13 (e). The INPC for the lower layer was found to be around 0.6 L^{-1} for this temperature. In the upper layer, n_{INP} went up to values slightly above 1 L^{-1}. These calculations have an error of ~~300%~~ a factor of three (dashed lines in Fig. 13 (e)) but nevertheless provide a guideline about the conditions of the cloud-relevant aerosol properties on the discussed day.

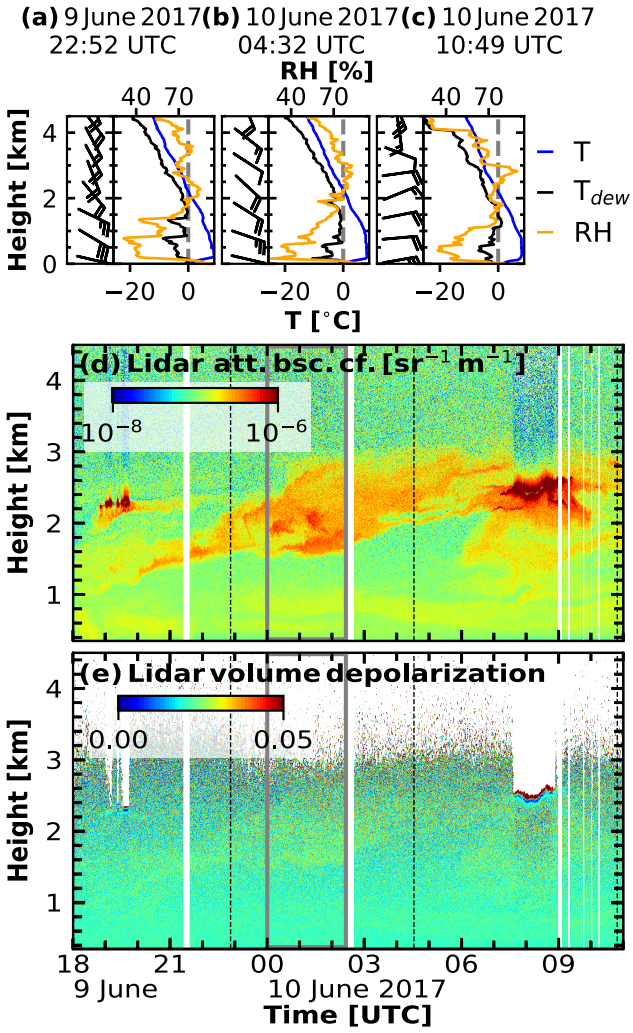

Figure 12. (a-c) same as Fig. 9 but for 9 June 2017 18:00 UTC – 10 June 2017 11:00 UTC up to 5 km. (d+e) measurements from Polly^{XT} between 9 June 2017, 18:00 UTC – 10 June 2017, 11:00 UTC. In (d) and (e), the 1064-nm attenuated backscatter coefficient and the 532-nm volume depolarization are shown, respectively. The black dashed lines mark the time of the radiosonde launches as shown in (a–c). The grey box indicates the period used for averaging in Fig. 13.

4.1.2 Ice cloud: 7 June 21:00 UTC – 8 June 09:00 UTC, ice floe camp

In Figure 14, we present the OCEANET measurements for the period from 7 June, 21:00 UTC to 8 June 2017, 09:00 UTC. The corresponding thermodynamic profiles from the radiosondes launched during this time period are shown in Fig. 15. In
495 Figure 16 (a), the Cloudnet target classification, together with the IWC (b), ice effective radius (c) and ice water path (d) are

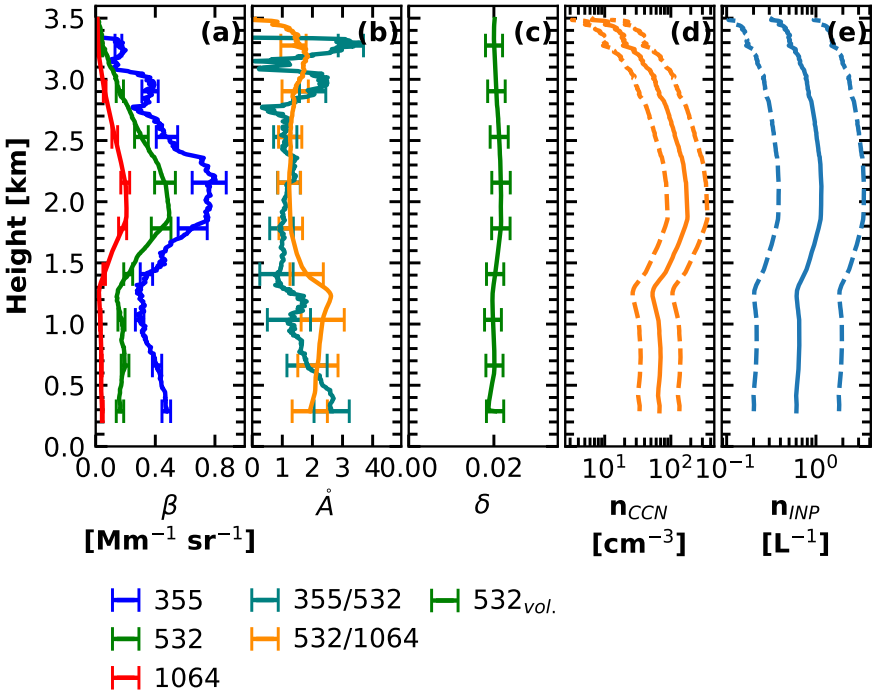

Figure 13. Averaged aerosol optical properties for the time period from 00:00 – 02:20 UTC on 10 June 2017 up to 3.5 km height. (a) aerosol backscatter coefficient for three wavelengths of 355 nm (blue), 532 nm (green) and 1064 nm (red). (b) Backscatter-related Ångstrom exponent for 355 nm to 532 nm (cyan) and for 532 nm to 1064 nm (orange). (c) 532 nm volume depolarization ratio. In (d) the retrieved CCN number concentration for C_2 = 10 cm^{-3} and d_2 = 0.9 and in (e) the INP number concentration for T =-15°C is shown together with the respective uncertainty (dashed lines) derived from the 53 nnm backscatter coefficient profile shown in (a).

shown. The ice water path is derived as the integral of the IWC for each profile. This period is chosen to illustrate the ~~fog~~ low-level stratus cloud detection algorithm and the retrieval of the ice effective radius.

At the beginning of the addressed time period, a low-level mixed-phase stratiform cloud reaching up to a height of 500 m is present. This layer is visible in both the cloud radar reflectivity as well as in the lidar attenuated backscatter data. Due to its high optical thickness, this cloud led almost continuously until 23:30 UTC to an attenuation of the lidar signal already close to cloud base (Fig. 14). Only occasionally, backscattered lidar signals from aerosols above the cloud were detected. During this period, the liquid water path varied between values of around 0 g m^{-2} for moments when the lidar was able to detect signal from above the cloud and values up to 100 g m^{-2} associated with periods when the lidar signal was attenuated already close to cloud base.

In Figure 17, the derived ~~fog~~ low-level stratus classification mask (below 165 m height) combined with a simplified Cloudnet target classification mask (above 165 m height) for this period is shown. Red areas depict detected ~~fog and~~ low level clouds. Blue and ~~Green~~ green data points indicate clear sky and aerosols, respectively. Though Polly^{XT} detected ~~fog~~ low-level stratus

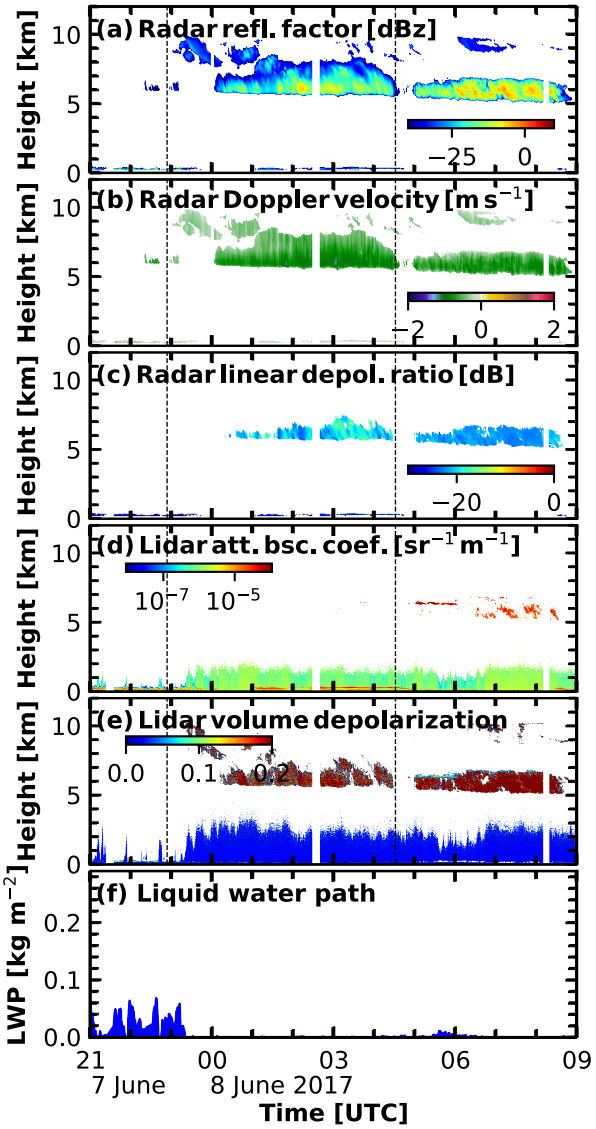

~~Same as Fig. 9 but for 7 June 2017 21:00 UTC – 8 June 2017 09:00 UTC.~~

Figure 14. Same as Fig. 10 but for 7 June 2017 21:00 UTC – 8 June 2017 09:00 UTC (note: the first and last launch shown in Fig. 15 was before the plotted profiles of the measurements start).

almost continuously during the case study, this affected the lidar signal most severely during the above mentioned period. After 23:30 UTC, the LWP showed values of around 10 g m^{-2} and the cloud lost most of its optical thickness so that the lidar was able to penetrate through the cloud.

~~Above the fog layer~~ Well above the low-level stratus some cirrus clouds formed around 22:30 UTC above 6000 m height. These transformed into a cirrostratus layer at 00:00 UTC which was present between 6000 and 10000 m height. Until around

~~Same as Fig. 10 but for 7 June 2017 21:00 UTC – 8 June 2017 09:00 UTC (note: the first and last launch shown in Fig. 15 was before the~~

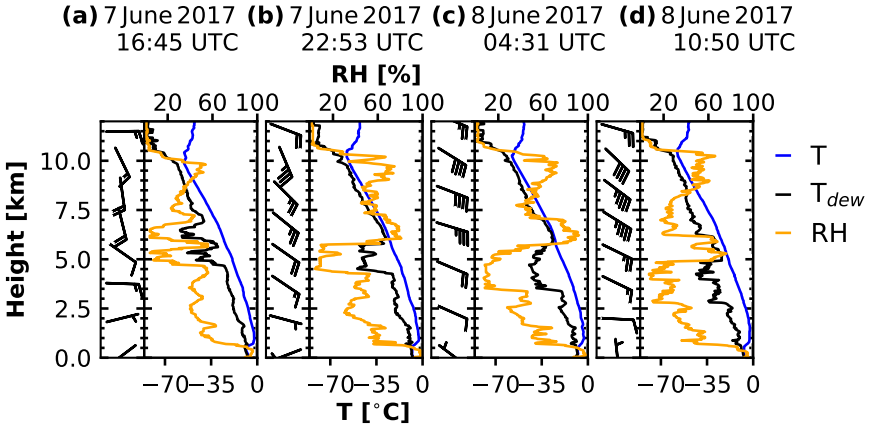

~~plotted profiles of the measurements start).~~

Figure 15. Same as Fig. 9 but for 7 June 2017 21:00 UTC – 8 June 2017 09:00 UTC up to 12 km height.

04:30 UTC, this cloud is classified as a pure ice cloud, characterized by LDR values of up to -15 dB and a constantly downward directed vertical velocity, with a tiny patch of detected liquid at around 03:30 UTC at 6100 m height.

At 04:30 UTC, the cirrostratus dissipated and another layer started to pass over Polarstern at around 05:00 UTC. This layer with coexisting liquid droplets and ice crystals extended from 5000 m up to 7000 m height. While the cloud radar reflectivity factor was higher in this layer compared to the first one, the cloud radar LDR decreased to values of below -20 dB. On top of this layer a supercooled liquid layer was detected by the lidar between 05:00 – 06:00 UTC, characterized by high attenuated backscatter coefficient and low values of linear depolarization ratio. Additionally, some regions with high linear depolarization ratio were detected by Polly^{XT} inside the cirrus after 06:30 UTC, probably associated to a mixture of supercooled droplets and ice crystals.

The IWC of the cirrostratus was ~~found to~~ in a range from 10^{-4} – 10^{-6} kg m^{-3} with lowest values at cloud top and highest values at cloud base. The ice effective radius ranged from 30 – 55 μm and its distribution follows the same pattern as the one of the IWC, as can be expected because both follow a similar reflectivity-temperature relationship.

4.2 Cloud statistics

In Figure 18, an overview about the statistical distribution of the cloud ~~and fog~~ occurrence during PS106 is given. In Figure 18 (a), daily statistics of the vertical distribution of ~~fog~~ low-level stratus is shown. In addition, the frequency of occurrence of ~~fog~~ this cloud type for each day is illustrated in Fig. 18 (b). ~~Fog~~ Low-level stratus was detected during a significant period of time on almost each day. The highest frequency of occurrence was observed while the Polarstern was surrounded by sea ice. Rather low values occurred while Polarstern was in the vicinity of Svalbard. In order to asses our retrieval of the low level clouds we plotted in comparison the frequency of occurrence of vertical visibility below 1 km.

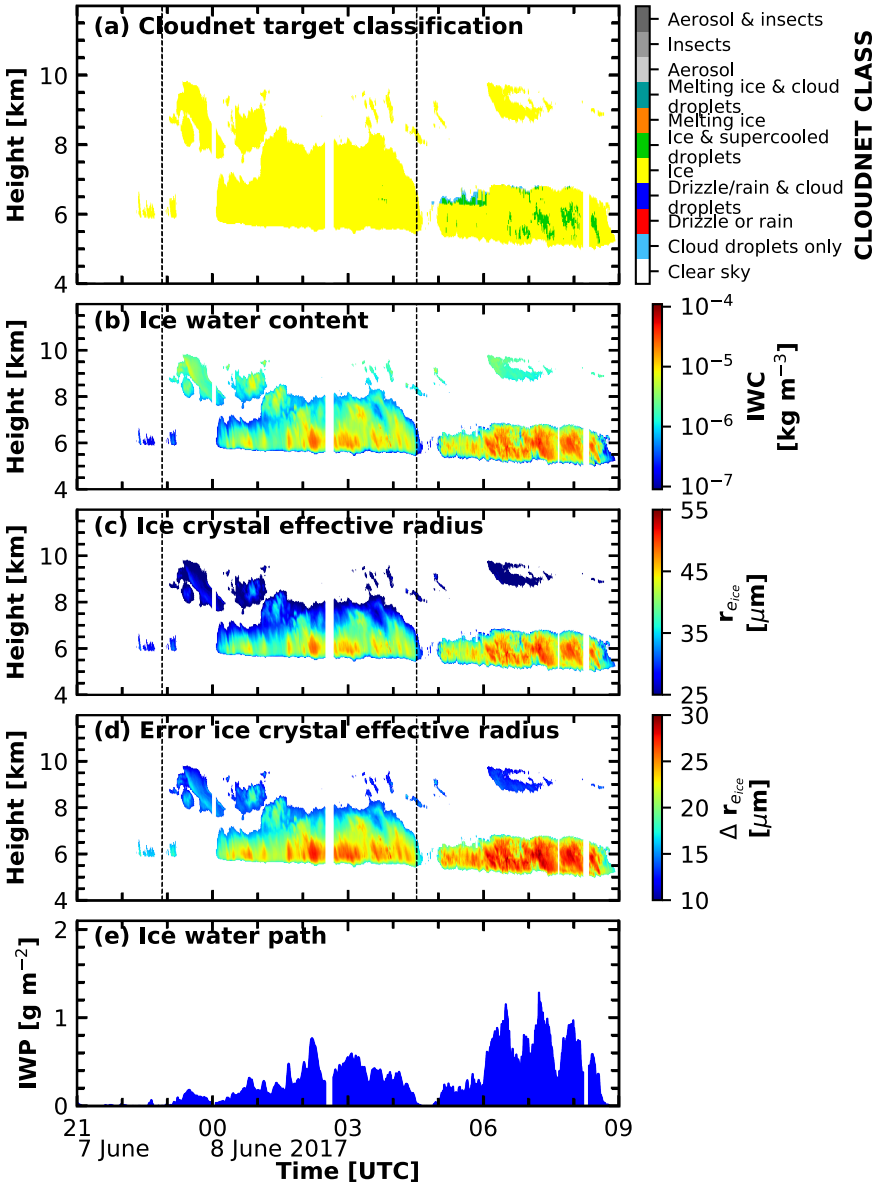

Figure 16. Cloudnet products for 7 June 2017, 21:00 UTC to 8 June 2017, 09:00 UTC: (a) target classification, (b) ice water content, (c) ice crystal effective radius, (d) uncertainty of the retrieved ice crystal effective radius as derived from error propagation, and (e) ice water path. The dashed lines mark the times of the radiosonde launches shown in Fig. 15 (note: the time of the first and last launch shown in Fig. 15 was before and after the presented time period).

Statistics of the cloud type occurrence are shown in Fig. 18 (c). The daily frequency of occurrence as well as the total distribution for the complete campaign of ~~fog~~ low level stratus clouds (purple), liquid clouds (orange), ice clouds (light blue),

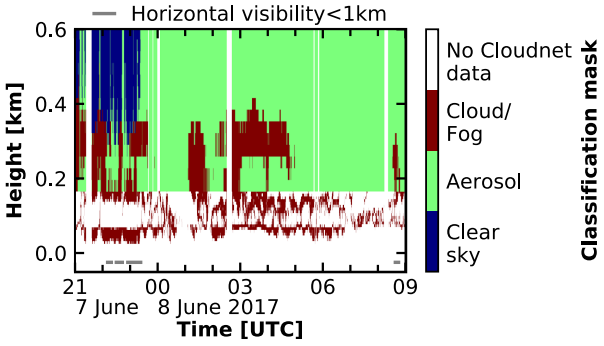

Figure 17. Low-level cloud mask for 7 June 2017 21:00 UTC – 8 June 2017 09:00 UTC derived from combining Polly^{XT} and Cloudnet data. Below 165 m height, red colors indicate when low-level stratus was detected using the signal-to-noise ratio (SNR) of the Polly^{XT} 532 nm near-field channel. Above 165 m height, a simplified version of the Cloudnet target classification mask is shown. Everything which was detected as cloud (either ice or liquid or mixed-phase) is masked in red. Blue depicts clear sky and green aerosols. The light-blue line at the bottom indicates periods when fog was detected by means of the visibility sensor aboard Polarstern.

mixed-phase clouds (green), multi-layer clouds (dark blue), and cloud-free situations (yellow) is shown. In addition, an analysis of the co-occurrence of ~~fog~~ low-level stratus and other cloud types was performed and is shown in the very right column of Fig. 18 (c). The rate of coexistence of the respective cloud type together with ~~fog~~ low-level stratus is indicated by a slightly varied color code.

In total, during 11% of the time cloud-free conditions were detected by Cloudnet during PS106. The two most prominent cloud types were multi-layer and mixed-phase clouds with an occurrence frequency of 38.5% and 36% of the observational time, respectively. Pure ice clouds were present for about 8% and pure liquid clouds for about 4.5% of the time, respectively. Single events of the new Cloudnet class ~~fog~~ low-level stratus cloud were detected during 2.5% of the time of the two month campaign. In addition, 27% of the observed liquid clouds and 48% of the ice clouds occurred simultaneously with ~~fog~~low-level stratus. Mixed-phase and multi-layer clouds were detected together with ~~fog~~ low level stratus clouds during 24% and 27% of their respective observational time.

In contrast to Nomokonova et al. (2019), who provided a statistical analysis of the cloud occurrence over Ny Ålesund, Svalbard, for the period between June 2016 and July 2017, we found a higher frequency of single layer mixed-phase clouds at the expense of cloud-free and single-layer liquid clouds when comparing the period of PS106. This may be due to a difference in turbulence as well as in a change of the cloud microphysics at locations surrounded by sea ice or open ocean (Young et al., 2016).

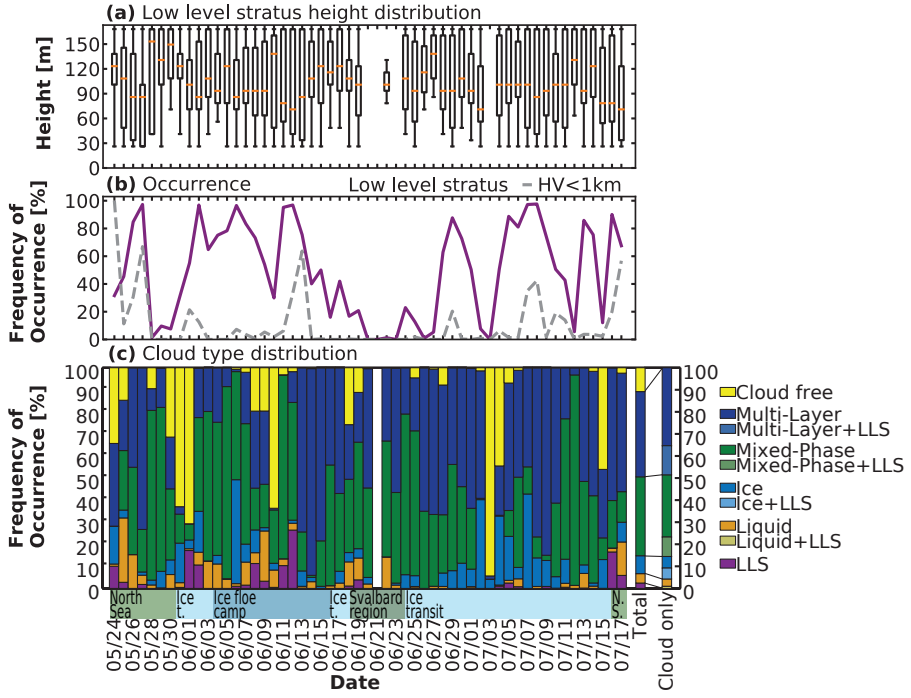

Figure 18. (a) daily height distribution of the detected ~~fog~~ low-level stratus during PS106 up to 165 m. (b) daily fraction of ~~fog~~ low-level stratus occurrence derived by Polly^{XT} measurements (purple) in comparison to horizontal visibility (HV) below 1 km (grey) . In (c) the cloud type statistics including ~~fog~~ low-level stratus clouds during PS106, determined by Cloudnet. Purple indicates the fraction when ~~fog~~ low-level stratus was determined, orange liquid clouds, light blue ice clouds, green mixed-phase clouds, dark blue multi-layer clouds and yellow cloud free periods. Each column except the last two represents one day of the campaign. The penultimate column represents the total distribution of the different cloud types. The last column distinguishes between the respective cloud type without ~~fog~~ low-level stratus detected (same color as in the other column) and with an additional ~~fog layer~~ low-level stratus detected below (slightly varied color). At the bottom a rough localization of Polarstern is annotated (green: North Sea (N.S.), light blue: Ice transit (Ice t.), dark blue: Ice floe camp, dark green: Svalbard region (Svalbard)).

5 Summary and Conclusions

A two-month campaign of RV Polarstern, including an extensive suite of ground-based remote sensing instruments of the OCEANET platform, has been conducted north- and northeast of ~~Savalbard~~ Svalbard in the Arctic summer of 2017. This study described in detail the deployed instrumentation and the applied processing schemes. Only few campaigns with a comparable equipment have been performed in recent years at these latitudes, e.g., ASCOS which took place from 2 August to 9 September 2008 (Tjernström et al., 2014) and ASCE in the Arctic summer and early autumn of 2014 (Tjernström et al., 2015). A new feature of PS106 was the deployment of a motion-stabilized vertically-pointing 35-GHz cloud radar during and the correction of the Doppler velocity subsequent to the cruise as specified in Sect. 3.1.

For an automatic, seamless analysis of cloud properties from the measured remote-sensing time series, the Cloudnet algorithm was utilized. In doing so, new products were developed and applied to the remote sensing data set from PS106. This was done in order to enable the continuous characterization of cloud turbulence by means of EDR, and to provide mass concentration and effective radius of ice crystals and liquid water droplets as future input for radiative transfer simulations. Though being well established, applying the Cloudnet algorithm to data from a remote-sensing supersite aboard a research vessel in the Arctic reveals new challenges. The movement of the ship has a significant effect on the measured vertical velocity of the cloud radar. To tackle this issue, the cloud radar was mounted on a stabilization platform to guarantee its vertical pointing. The vertical velocity ~~dataset~~ data set was corrected for the heave rate of the ship in a post-processing procedure subsequent to the cruise.

The motion stabilization was evaluated by means of a small single board computer mounted on the cloud radar rack. The IMU of the mini computer measured the residual of the pitch and roll movement after stabilization. We found a good stabilization during ice breaking conditions with a leveling precision of $\pm 0.5°$. During rough sea however the displacement from zenith was larger, up to $\pm 1°$. Under the strong wave conditions during these time periods it needs also to be considered, that the IMU of the orientation sensor used for the cloud radar is based on so called MEMS (Micro-Electro-Mechanical Systems). Such devices are based on spring-mounted capacitor plates and thus measured pitch and roll angles are affected by translational motions like engine vibrations etc. As these effects were not investigated in the frame of our study, we conclude that the actual vertical-pointing uncertainty range, especially on the open sea, was lower than the one reported by the MEMS sensors, i.e., better than $\pm 1°$.

Using the corrected vertical velocities from the cloud radar, the eddy dissipation rates were calculated ~~.~~ and evaluated against in-cloud turbulence measurements done by means of a tethered balloon. This intercomparison revealed a good agreement between both approaches where the values where within the estimated uncertainty and the expected difference due to the spacial distance. Nevertheless the tethered balloon approach seems to be the more reliable one, given the smaller standard deviation.

Based on published retrievals of visible extinction coefficient and ice water content, ~~the~~ a new approach to derive the effective radius of the ice crystals was introduced. The associated uncertainties, estimated by error propagation, of the ice crystal effective radii are presented in Fig. 16 (d). On average the uncertainty is about 50% of the size of the radii themselves which reflects the strong influence of uncertainties in the underlying observational data on the retrieval. Given the challenges in estimating the effective radius of ice crystals on a continuous basis on the one hand and the necessity of having such values, e.g., for radiative transfer calculations, on the other hand, we consider this estimate to be still in a reasonable range. In Figure 19, the histogram of the effective radius for full PS106 is shown. Values range from 20 – 60 μm, with a peak at around 50 μm. This is consistent with other studies of ice effective radius (e.g., Blanchard et al., 2017).

This study revealed in addition the relevance of the lowest detection limit of remote sensing instruments on the representativity of Arctic-cloud statistics. Cloudnet is configured to have its lowest range gate at the lowest detection altitude of the cloud radar, which was 165 m above the ocean surface for PS106. Lower-level cloud layers are thus not identifiable within Cloudnet. In our study, lower cloud structures were identified using the SNR measured by the lidar Polly^{XT}. This ability has been used

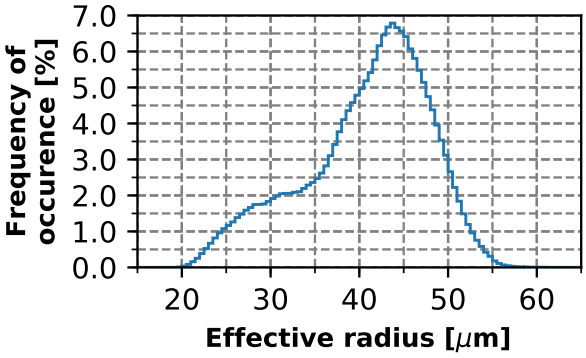

Figure 19. Histogram of the ice particle effective radius for PS106. Integration over x yields 100%.

to study the occurrence of ~~fog and~~ low-level stratus clouds below the first Cloudnet range gate. ~~So~~ Sotiropoulou et al. (2014) used a combination of cloud radar and ceilometer measurements to study stratiform Arctic clouds and found that most stable, surface coupled clouds have a cloud base below 200 m. Yet, so far such clouds have not been considered in ~~most~~ many Arctic cloud climatologies derived by remote sensing instruments. Liu et al. (2012) for example defined low-level clouds as those between 0 and 2000 m, with 960 m above the ground being the height where surface contamination effects on Cloudsat become insignificant, and using a vertical resolution of 240 m. Shupe (2011) summarized cloud statistics from several multi-year data sets derived from ground-based remote-sensing observations for different sites in the Arctic. ~~They~~ He specified a height dependence of cloud occurrence down to 300 m by using a combination of lidar and radar. Below 300 m, however, ~~they~~ he provided information about cloud occurrence but without any further specification of the cloud base. Even airborne remote sensing instruments suffer from the strong ground clutter and thus struggle to deliver information about cloud occurrence below 150 m height above the surface (Mech et al., 2019). The autonomous buoys of the IAOOS network equipped with a microlidar observed in 2014 and 2015 in the Arctic clouds with a base height below 500 m during 60 % of their observational time Mariage et al. (2017).

Our study shows that a higher vertical resolution and reliable signal from very low altitudes is required to characterize the lowest-level cloud layer which occur between approximately 50 m and 165 m above ground. Such clouds stay undetected for ground-based in-situ sensors (because they are too high) as well as for most automatized ground-based remote sensing instruments (because they are too low). Future radiative transfer studies should show what the effect of the lowest-level clouds, which occurred during 25% of the observation time, is on the radiation budget of the region where PS106 was performed.

Future work will confront the observed cloud macro- and microphysical properties as well as the EDR with high resolution model simulations along the PS106 track that have been carried out in the framework of $(AC)^3$. The herein introduced remote sensing techniques will also be applied to the ~~dataset~~ data set of the currently ongoing one-year polar ice drift of RV Polarstern during the MOSAiC project (Schiermeier, 2019), thus providing an unprecedented data set of Arctic aerosol and mixed-phase

clouds. This data set will substantially contribute to our understanding of the role of clouds in the current warming of the Arctic climate system.

Code and data availability. ~~The trajectory analysis software "trace" as used for this publication is available under Radenz and Seifert (2019) . The most recent version is available via GitHub: https://github.com/martin-rdz/trace (last access: 04.09.2019).~~ The radiosonde data is available by Schmithüsen (2017a) (PS106.1) and Schmithüsen (2017b) (PS106.2). The lidar measurements are available by Griesche et al. (2019c), the cloud radar measurements by Griesche et al. (2020b). The Cloudnet data set is available by Griesche et al. (2020a) and related data sets. The publication of the low level stratus cloud data set is in progress Griesche and Seifert (2020).

Author contributions. PS, RE and JB designed the OCEANET measurements and PS, RE, JB, MR and HG prepared the instruments. HG, RE, MR and CB operated the OCEANET instruments aboard Polarstern. PS and HG processed the data with Cloudnet and developed the low level stratus detection algorithm. HG performed the heave correction and developed the EDR and ice crystal effective radius retrieval with supervision from PS, RE and JB. HB, ZY, and AA provided lidar-based data processing for retrieval of aerosol optical and microphysical properties. AM provided support in the data analysis and manuscript preparation. HG drafted the manuscript with contributions from all co-authors.

Competing interests. The authors declare that they have no conflict of interest.

Acknowledgements. We gratefully acknowledge the funding by the Deutsche Forschungsgemeinschaft (DFG, German Research Foundation) – Project Number 268020496 – TRR 172, within the Transregional Collaborative Research Center "ArctiC Amplification: Climate Relevant Atmospheric and SurfaCe Processes, and Feedback Mechanisms (AC)3". We thank the Alfred Wegener Institute and R/V Polarstern crew and captain for their support (AWI_PS106_00). We also thank the University on Cologne for providing us with the MWR retrieval for Ny-Ålesund, Svalbard, Norway. Authors acknowledge also support through ACTRIS-2 under grant agreement no. 654109 from the European Union's Horizon 2020 research and innovation programme.

References

Achtert, P., Brooks, I. M., Brooks, B. J., Moat, B. I., Prytherch, J., Persson, P. O. G., and Tjernström, M.: Measurement of wind profiles by motion-stabilised ship-borne Doppler lidar, Atmospheric Measurement Techniques, 8, 4993–5007, https://doi.org/10.5194/amt-8-4993-2015, https://www.atmos-meas-tech.net/8/4993/2015/, 2015.

Anderson, G., Clough, S., Kneizys, F., Chetwynd, J., and Shettle, E.: AFGL atmospheric constituent profiles (0–120 km), techreport, AIR FORCE GEOPHYSICS LAB HANSCOM AFB MA, https://apps.dtic.mil/dtic/tr/fulltext/u2/a175173.pdf, 1986.

Baars, H., Ansmann, A., Althausen, D., Engelmann, R., Artaxo, P., Pauliquevis, T., and Souza, R.: Further evidence for significant smoke transport from Africa to Amazonia, Geophysical Research Letters, 38, https://doi.org/10.1029/2011GL049200, https://agupubs.onlinelibrary.wiley.com/doi/abs/10.1029/2011GL049200, 2011.

Baars, H., Ansmann, A., Althausen, D., Engelmann, R., Heese, B., Müller, D., Artaxo, P., Paixao, M., Pauliquevis, T., and Souza, R.: Aerosol profiling with lidar in the Amazon Basin during the wet and dry season, Journal of Geophysical Research: Atmospheres, 117, https://doi.org/10.1029/2012JD018338, https://agupubs.onlinelibrary.wiley.com/doi/abs/10.1029/2012JD018338, 2012.

Baars, H., Kanitz, T., Engelmann, R., Althausen, D., Heese, B., Komppula, M., Preißler, J., Tesche, M., Ansmann, A., Wandinger, U., Lim, J.-H., Ahn, J. Y., Stachlewska, I. S., Amiridis, V., Marinou, E., Seifert, P., Hofer, J., Skupin, A., Schneider, F., Bohlmann, S., Foth, A., Bley, S., Pfüller, A., Giannakaki, E., Lihavainen, H., Viisanen, Y., Hooda, R. K., Pereira, S. N., Bortoli, D., Wagner, F., Mattis, I., Janicka, L., Markowicz, K. M., Achtert, P., Artaxo, P., Pauliquevis, T., Souza, R. A. F., Sharma, V. P., van Zyl, P. G., Beukes, J. P., Sun, J., Rohwer, E. G., Deng, R., Mamouri, R.-E., and Zamorano, F.: An overview of the first decade of Polly^{NET}: an emerging network of automated Raman-polarization lidars for continuous aerosol profiling, Atmospheric Chemistry and Physics, 16, 5111–5137, https://doi.org/10.5194/acp-16-5111-2016, https://www.atmos-chem-phys.net/16/5111/2016/, 2016.

Baars, H., Seifert, P., Engelmann, R., and Wandinger, U.: Target categorization of aerosol and clouds by continuous multiwavelength-polarization lidar measurements, Atmospheric Measurement Techniques, 10, 3175–3201, https://doi.org/10.5194/amt-10-3175-2017, https://www.atmos-meas-tech.net/10/3175/2017/, 2017.

Barker, H., Stephens, G., Partain, P., Bergman, J., Bonnel, B., Campana, K., Clothiaux, E., Clough, S., Cusack, S., Delamere, J., Edwards, J., Evans, K., Fouquart, Y., Freidenreich, S., Galin, V., Hou, Y., Kato, S., Li, J., EJ, M., and Yang, F.: Assessing 1D Atmospheric Solar Radiative Transfer Models: Interpretation and Handling of Unresolved Clouds, Journal of Climate - J CLIMATE, 16, 2676–2699, https://doi.org/10.1175/1520-0442(2003)016<2676:ADASRT>2.0.CO;2, 2003.

Barrientos Velasco, C., Deneke, H., Griesche, H., Seifert, P., Engelmann, R., and Macke, A.: Spatiotemporal variability of shortwave radiation introduced by clouds over the Arctic sea ice, Atmospheric Measurement Techniques Discussions, 2019, 1–36, https://doi.org/10.5194/amt-2019-231, https://www.atmos-meas-tech-discuss.net/amt-2019-231/, 2019.

Barrientos Velasco, C., Deneke, H., Griesche, H., Seifert, P., Engelmann, R., and Macke, A.: Spatiotemporal variability of solar radiation introduced by clouds over Arctic sea ice, Atmospheric Measurement Techniques, 13, 1757–1775, https://doi.org/10.5194/amt-13-1757-2020, https://www.atmos-meas-tech.net/13/1757/2020/, 2020.

Bühl, J., Ansmann, A., Seifert, P., Baars, H., and Engelmann, R.: Toward a quantitative characterization of heterogeneous ice formation with lidar/radar: Comparison of CALIPSO/CloudSat with ground-based observations, Geophys. Res. Lett., 40, 4404–4408, https://doi.org/10.1002/grl.50792, https://doi.org/10.1002/grl.50792, 2013.

Blanchard, Y., Royer, A., O'Neill, N. T., Turner, D. D., and Eloranta, E. W.: Thin ice clouds in the Arctic: cloud optical depth and particle size retrieved from ground-based thermal infrared radiometry, Atmospheric Measurement Techniques, 10, 2129–2147, https://doi.org/10.5194/amt-10-2129-2017, https://www.atmos-meas-tech.net/10/2129/2017/, 2017.

Bohlmann, S., Baars, H., Radenz, M., Engelmann, R., and Macke, A.: Ship-borne aerosol profiling with lidar over the Atlantic Ocean: from pure marine conditions to complex dust–smoke mixtures, Atmospheric Chemistry and Physics, 18, 9661–9679, https://doi.org/10.5194/acp-18-9661-2018, https://www.atmos-chem-phys.net/18/9661/2018/, 2018.

Borque, P., Luke, E., and Kollias, P.: On the unified estimation of turbulence eddy dissipation rate using Doppler cloud radars and lidars, Journal of Geophysical Research: Atmospheres, 121, 5972–5989, https://doi.org/10.1002/2015JD024543, https://agupubs.onlinelibrary.wiley.com/doi/abs/10.1002/2015JD024543, 2016.

Bühl, J., Seifert, P., Myagkov, A., and Ansmann, A.: Measuring ice- and liquid-water properties in mixed-phase cloud layers at the Leipzig Cloudnet station, Atmospheric Chemistry and Physics, 16, 10 609–10 620, https://doi.org/10.5194/acp-16-10609-2016, https://www.atmos-chem-phys.net/16/10609/2016/, 2016.

Caughey, S. J., Wyngaard, J. C., and Kaimal, J. C.: Turbulence in the Evolving Stable Boundary Layer, Journal of the Atmospheric Sciences, 36, 1041–1052, 1979.

Clough, S., Shephard, M., Mlawer, E., Delamere, J., Iacono, M., Cady-Pereira, K., Boukabara, S., and Brown, P.: Atmospheric radiative transfer modeling: a summary of the AER codes, Journal of Quantitative Spectroscopy and Radiative Transfer, 91, 233 – 244, https://doi.org/https://doi.org/10.1016/j.jqsrt.2004.05.058, http://www.sciencedirect.com/science/article/pii/S0022407304002158, 2005.

Curry, J. A., Hobbs, P. V., King, M. D., Randall, D. A., Minnis, P., Isaac, G. A., Pinto, J. O., Uttal, T., Bucholtz, A., Cripe, D. G., Gerber, H., Fairall, C. W., Garrett, T. J., Hudson, J., Intrieri, J. M., Jakob, C., Jensen, T., Lawson, P., Marcotte, D., Nguyen, L., Pilewskie, P., Rangno, A., Rogers, D. C., Strawbridge, K. B., Valero, F. P. J., Williams, A. G., and Wylie, D.: FIRE Arctic Clouds Experiment, Bulletin of the American Meteorological Society, 81, 5–30, https://doi.org/10.1175/1520-0477(2000)081<0005:FACE>2.3.CO;2, https://doi.org/10.1175/1520-0477(2000)081<0005:FACE>2.3.CO;2, 2000.

Dai, G., Althausen, D., Hofer, J., Engelmann, R., Seifert, P., Bühl, J., Mamouri, R.-E., Wu, S., and Ansmann, A.: Calibration of Raman lidar water vapor profiles by means of AERONET photometer observations and GDAS meteorological data, Atmospheric Measurement Techniques, 11, 2735–2748, https://doi.org/10.5194/amt-11-2735-2018, https://www.atmos-meas-tech.net/11/2735/2018/, 2018.

de Boer, G., Eloranta, E. W., and Shupe, M. D.: Arctic Mixed-Phase Stratiform Cloud Properties from Multiple Years of Surface-Based Measurements at Two High-Latitude Locations, Journal of the Atmospheric Sciences, 66, 2874–2887, https://doi.org/10.1175/2009JAS3029.1, https://doi.org/10.1175/2009JAS3029.1, 2009.

Delanoë, J., Protat, A., Bouniol, D., Heymsfield, A., Bansemer, A., and Brown, P.: The Characterization of Ice Cloud Properties from Doppler Radar Measurements, Journal of Applied Meteorology and Climatology, 46, 1682–1698, https://doi.org/10.1175/JAM2543.1, https://doi.org/10.1175/JAM2543.1, 2007.

DeMott, P. J., Prenni, A. J., Liu, X., Kreidenweis, S. M., Petters, M. D., Twohy, C. H., Richardson, M. S., Eidhammer, T., and Rogers, D. C.: Predicting global atmospheric ice nuclei distributions and their impacts on climate, Proceedings of the National Academy of Sciences, 107, 11 217–11 222, https://doi.org/10.1073/pnas.0910818107, https://www.pnas.org/content/107/25/11217, 2010.

Ebell, K., Nomokonova, T., Maturilli, M., and Ritter, C.: Radiative Effect of Clouds at Ny-Ålesund, Svalbard, as Inferred from Ground-Based Remote Sensing Observations, Journal of Applied Meteorology and Climatology, 59, 3–22, https://doi.org/10.1175/JAMC-D-19-0080.1, https://doi.org/10.1175/JAMC-D-19-0080.1, 2019.

Egerer, U., Gottschalk, M., Siebert, H., Ehrlich, A., and Wendisch, M.: The new BELUGA setup for collocated turbulence and radiation measurements using a tethered balloon: first applications in the cloudy Arctic boundary layer, Atmospheric Measurement Techniques, 12, 4019–4038, https://doi.org/10.5194/amt-12-4019-2019, https://www.atmos-meas-tech.net/12/4019/2019/, 2019.

Ehrlich, A., Wendisch, M., Lüpkes, C., Buschmann, M., Bozem, H., Chechin, D., Clemen, H.-C., Dupuy, R., Eppers, O., Hartmann, J., Herber, A., Jäkel, E., Järvinen, E., Jourdan, O., Kästner, U., Kliesch, L.-L., Köllner, F., Mech, M., Mertes, S., Neuber, R., Ruiz-Donoso, E., Schnaiter, M., Schneider, J., Stapf, J., and Zanatta, M.: A comprehensive in situ and remote sensing data set from the Arctic CLoud Observations Using airborne measurements during polar Day (ACLOUD) campaign, Earth System Science Data, 11, 1853–1881, https://doi.org/10.5194/essd-11-1853-2019, https://www.earth-syst-sci-data.net/11/1853/2019/, 2019.

Engelmann, R., Kanitz, T., Baars, H., Heese, B., Althausen, D., Skupin, A., Wandinger, U., Komppula, M., Stachlewska, I. S., Amiridis, V., Marinou, E., Mattis, I., Linné, H., and Ansmann, A.: The automated multiwavelength Raman polarization and water-vapor lidar Polly^{XT}: the neXT generation, Atmospheric Measurement Techniques, 9, 1767–1784, https://doi.org/10.5194/amt-9-1767-2016, https://www.atmos-meas-tech.net/9/1767/2016/, 2016.

Foth, A., Kanitz, T., Engelmann, R., Baars, H., Radenz, M., Seifert, P., Barja, B., Fromm, M., Kalesse, H., and Ansmann, A.: Vertical aerosol distribution in the southern hemispheric midlatitudes as observed with lidar in Punta Arenas, Chile (53.2° S and 70.9° W), during ALPACA, Atmospheric Chemistry and Physics, 19, 6217–6233, https://doi.org/10.5194/acp-19-6217-2019, https://www.atmos-chem-phys.net/19/6217/2019/, 2019.

Frehlich, R. and Cornman, L.: Estimating Spatial Velocity Statistics with Coherent Doppler Lidar, Journal of Atmospheric and Oceanic Technology, 19, 355–366, https://doi.org/10.1175/1520-0426-19.3.355, https://doi.org/10.1175/1520-0426-19.3.355, 2002.

Frisch, A. S., Feingold, G., Fairall, C. W., Uttal, T., and Snider, J. B.: On cloud radar and microwave radiometer measurements of stratus cloud liquid water profiles, Journal of Geophysical Research: Atmospheres, 103, 23 195–23 197, https://doi.org/10.1029/98JD01827, https://agupubs.onlinelibrary.wiley.com/doi/abs/10.1029/98JD01827, 1998.

Frisch, S., Shupe, M., Djalalova, I., Feingold, G., and Poellot, M.: The Retrieval of Stratus Cloud Droplet Effective Radius with Cloud Radars, Journal of Atmospheric and Oceanic Technology, 19, 835–842, https://doi.org/10.1175/1520-0426(2002)019<0835:TROSCD>2.0.CO;2, https://doi.org/10.1175/1520-0426(2002)019<0835:TROSCD>2.0.CO;2, 2002.

GDAS: Global Data Assimilation System, Tech. rep., NOAA, https://www.ncdc.noaa.gov/data-access/model-data/model-datasets/global-data-assimilation-system-gdas.

Goosse, H., Kay, J. E., Armour, K. C., Bodas-Salcedo, A., Chepfer, H., Docquier, D., Jonko, A., Kushner, P. J., Lecomte, O., Massonnet, F., Park, H.-S., Pithan, F., Svensson, G., and Vancoppenolle, M.: Quantifying climate feedbacks in polar regions, Nature Communications, 9, 1919, https://doi.org/10.1038/s41467-018-04173-0, 2018.

Görsdorf, U., Lehmann, V., Bauer-Pfundstein, M., Peters, G., Vavriv, D., Vinogradov, V., and Volkov, V.: A 35-GHz Polarimetric Doppler Radar for Long-Term Observations of Cloud Parameters—Description of System and Data Processing, Journal of Atmospheric and Oceanic Technology, 32, 675–690, https://doi.org/10.1175/JTECH-D-14-00066.1, https://doi.org/10.1175/JTECH-D-14-00066.1, 2015.

Granskog, M. A., Fer, I., Rinke, A., and Steen, H.: Atmosphere-Ice-Ocean-Ecosystem Processes in a Thinner Arctic Sea Ice Regime: The Norwegian Young Sea ICE (N-ICE2015) Expedition, J. Geophys. Res. Oceans, 123, 1586–1594, https://doi.org/10.1002/2017jc013328, https://doi.org/10.1002/2017JC013328, 2018.

Griesche, H. and Seifert, P.: Low level stratus clouds during PS106, 2020.

Griesche, H., Seifert, P., Engelmann, R., Radenz, M., and Bühl, J.: OCEANET Cloud radar Mira-35 during POLARSTERN cruise PS106, https://doi.org/10.1594/PANGAEA.899895, https://doi.org/10.1594/PANGAEA.899895, 2019a.

Griesche, H., Seifert, P., Engelmann, R., Radenz, M., and Bühl, J.: OCEANET-ATMOSPHERE Mircowave Radiometer Hatpro during POLARSTERN cruise PS106, https://doi.org/10.1594/PANGAEA.899898, https://doi.org/10.1594/PANGAEA.899898, 2019b.

Griesche, H., Seifert, P., Engelmann, R., Radenz, M., and Bühl, J.: OCEANET-ATMOSPHERE PollyXT measurements during POLARSTERN cruise PS106, https://doi.org/10.1594/PANGAEA.899458, https://doi.org/10.1594/PANGAEA.899458, 2019c.

Griesche, H., Seifert, P., Engelmann, R., Radenz, M., and Bühl, J.: Cloudnet target classification during POLARSTERN cruise PS106 classification, https://doi.org/10.1594/PANGAEA.919463, https://doi.pangaea.de/10.1594/PANGAEA.919463, 2020a.

Griesche, H., Seifert, P., Engelmann, R., Radenz, M., and Bühl, J.: OCEANET-ATMOSPHERE Cloud radar Mira-35 during PS106, https://doi.org/10.1594/PANGAEA.919556, https://doi.pangaea.de/10.1594/PANGAEA.919556, 2020b.

Griesche, H., Seifert, P., Engelmann, R., Radenz, M., and Bühl, J.: OCEANET-ATMOSPHERE Mircowave Radiometer Hatpro during POLARSTERN cruise PS106, https://doi.org/10.1594/PANGAEA.919359, https://doi.pangaea.de/10.1594/PANGAEA.919359, 2020c.

Heese, B., Flentje, H., Althausen, D., Ansmann, A., and Frey, S.: Ceilometer lidar comparison: backscatter coefficient retrieval and signal-to-noise ratio determination, Atmospheric Measurement Techniques, 3, 1763–1770, https://doi.org/10.5194/amt-3-1763-2010, https://www.atmos-meas-tech.net/3/1763/2010/, 2010.

Hogan, R. and O'Connor, E.: Facilitating cloud radar and lidar algorithms: the Cloudnet Instrument Synergy / Target Categorization product, Tech. rep., http://www.met.rdg.ac.uk/~swrhgnrj/publications/categorization.pdf, 2004.

Hogan, R. J., Mittermaier, M. P., and Illingworth, A. J.: The Retrieval of Ice Water Content from Radar Reflectivity Factor and Temperature and Its Use in Evaluating a Mesoscale Model, Journal of Applied Meteorology and Climatology, 45, 301–317, https://doi.org/10.1175/JAM2340.1, https://doi.org/10.1175/JAM2340.1, 2006.

Iacono, M. J., Delamere, J. S., Mlawer, E. J., Shephard, M. W., Clough, S. A., and Collins, W. D.: Radiative forcing by long-lived greenhouse gases: Calculations with the AER radiative transfer models, Journal of Geophysical Research: Atmospheres, 113, https://doi.org/10.1029/2008JD009944, https://agupubs.onlinelibrary.wiley.com/doi/abs/10.1029/2008JD009944, 2008.

Illingworth, A. J., Hogan, R. J., O'Connor, E., Bouniol, D., Brooks, M. E., Delanoé, J., Donovan, D. P., Eastment, J. D., Gaussiat, N., Goddard, J. W. F., Haeffelin, M., Baltink, H. K., Krasnov, O. A., Pelon, J., Piriou, J.-M., Protat, A., Russchenberg, H. W. J., Seifert, A., Tompkins, A. M., van Zadelhoff, G.-J., Vinit, F., Willén, U., Wilson, D. R., and Wrench, C. L.: Cloudnet, Bulletin of the American Meteorological Society, 88, 883–898, https://doi.org/10.1175/BAMS-88-6-883, https://doi.org/10.1175/BAMS-88-6-883, 2007.

Jacob, D. J., Crawford, J. H., Maring, H., Clarke, A. D., Dibb, J. E., Emmons, L. K., Ferrare, R. A., Hostetler, C. A., Russell, P. B., Singh, H. B., Thompson, A. M., Shaw, G. E., McCauley, E., Pederson, J. R., and Fisher, J. A.: The Arctic Research of the Composition of the Troposphere from Aircraft and Satellites (ARCTAS) mission: design, execution, and first results, Atmospheric Chemistry and Physics, 10, 5191–5212, https://doi.org/10.5194/acp-10-5191-2010, https://www.atmos-chem-phys.net/10/5191/2010/, 2010.

Jensen, M. P., Holdridge, D. J., Survo, P., Lehtinen, R., Baxter, S., Toto, T., and Johnson, K. L.: Comparison of Vaisala radiosondes RS41 and RS92 at the ARM Southern Great Plains site, Atmospheric Measurement Techniques, 9, 3115–3129, https://doi.org/10.5194/amt-9-3115-2016, https://www.atmos-meas-tech.net/9/3115/2016/, 2016.

Kaimal, J. C., Wyngaard, J. C., Haugen, D. A., Coté, O. R., Izumi, Y., Caughey, S. J., and Readings, C. J.: Turbulence Structure in the Convective Boundary Layer, Journal of the Atmospheric Sciences, 33, 2152–2169, https://doi.org/10.1175/1520-0469(1976)033<2152:TSITCB>2.0.CO;2, https://doi.org/10.1175/1520-0469(1976)033<2152:TSITCB>2.0.CO;2, 1976.

Kalesse, H. and Kollias, P.: Climatology of High Cloud Dynamics Using Profiling ARM Doppler Radar Observations, Journal of Climate, 26, 6340–6359, https://doi.org/10.1175/JCLI-D-12-00695.1, https://doi.org/10.1175/JCLI-D-12-00695.1, 2013.

Kalesse, H., de Boer, G., Solomon, A., Oue, M., Ahlgrimm, M., Zhang, D., Shupe, M. D., Luke, E., and Protat, A.: Understanding Rapid Changes in Phase Partitioning between Cloud Liquid and Ice in Stratiform Mixed-Phase Clouds: An Arctic Case Study, Monthly Weather Review, 144, 4805–4826, https://doi.org/10.1175/MWR-D-16-0155.1, https://doi.org/10.1175/MWR-D-16-0155.1, 2016a.

Kalesse, H., Szyrmer, W., Kneifel, S., Kollias, P., and Luke, E.: Fingerprints of a riming event on cloud radar Doppler spectra: observations and modeling, Atmospheric Chemistry and Physics, 16, 2997–3012, https://doi.org/10.5194/acp-16-2997-2016, https://www.atmos-chem-phys.net/16/2997/2016/, 2016b.

Kanitz, T., Ansmann, A., Engelmann, R., and Althausen, D.: North-south cross sections of the vertical aerosol distribution over the Atlantic Ocean from multiwavelength Raman/polarization lidar during Polarstern cruises, Journal of Geophysical Research: Atmospheres, 118, 2643–2655, https://doi.org/10.1002/jgrd.50273, https://agupubs.onlinelibrary.wiley.com/doi/abs/10.1002/jgrd.50273, 2013a.

Kanitz, T., Ansmann, A., Seifert, P., Engelmann, R., Kalisch, J., and Althausen, D.: Radiative effect of aerosols above the northern and southern Atlantic Ocean as determined from shipborne lidar observations, Journal of Geophysical Research: Atmospheres, 118, 12,556–12,565, https://doi.org/10.1002/2013JD019750, https://agupubs.onlinelibrary.wiley.com/doi/abs/10.1002/2013JD019750, 2013b.

Kecorius, S., Vogl, T., Paasonen, P., Lampilahti, J., Rothenberg, D., Wex, H., Zeppenfeld, S., van Pinxteren, M., Hartmann, M., Henning, S., Gong, X., Welti, A., Kulmala, M., Stratmann, F., Herrmann, H., and Wiedensohler, A.: New particle formation and its effect on CCN abundance in the summer Arctic: a case study during PS106 cruise, Atmospheric Chemistry and Physics Discussions, 2019, 1–41, https://doi.org/10.5194/acp-2019-600, https://www.atmos-chem-phys-discuss.net/acp-2019-600/, 2019.

Klepp, C., Michel, S., Protat, A., Burdanowitz, J., Albern, N., Kahnert, M., Dahl, A., Louf, V., Bakan, S., and Buehler, S. A.: OceanRAIN, a new in-situ shipboard global ocean surface-reference dataset of all water cycle components, Sci Data, 5, 180 122, https://doi.org/10.1038/sdata.2018.122, 2018.

Knudsen, E. M., Heinold, B., Dahlke, S., Bozem, H., Crewell, S., Heygster, G., Kunkel, D., Maturilli, M., Mech, M., Rinke, A., Schmithüsen, H., Ehrlich, A., Macke, A., Lüpkes, C., and Wendisch, M.: Synoptic development during the ACLOUD/PASCAL field campaign near Svalbard in spring 2017, Atmospheric Chemistry and Physics Discussions, 2018, 1–46, https://doi.org/10.5194/acp-2018-494, https://www.atmos-chem-phys-discuss.net/acp-2018-494/, 2018.

Löhnert, U. and Crewell, S.: Accuracy of cloud liquid water path from ground-based microwave radiometry 1. Dependency on cloud model statistics, Radio Science, 38, https://doi.org/10.1029/2002RS002654, https://agupubs.onlinelibrary.wiley.com/doi/abs/10.1029/2002RS002654, 2003.

Liu, Y., Key, J. R., Ackerman, S. A., Mace, G. G., and Zhang, Q.: Arctic cloud macrophysical characteristics from CloudSat and CALIPSO, Remote Sensing of Environment, 124, 159 – 173, https://doi.org/10.1016/j.rse.2012.05.006, http://www.sciencedirect.com/science/article/pii/S003442571200209X, 2012.

Lothon, M., Lenschow, D. H., Leon, D., and Vali, G.: Turbulence measurements in marine stratocumulus with airborne Doppler radar, Quarterly Journal of the Royal Meteorological Society, 131, 2063–2080, https://doi.org/10.1256/qj.04.131, https://rmets.onlinelibrary.wiley.com/doi/abs/10.1256/qj.04.131, 2005.

Macke, A. and Flores, H.: The Expeditions PS106/1 and 2 of the Research Vessel POLARSTERN to the Arctic Ocean in 2017, https://doi.org/10.2312/BzPM_0719_2018, 2018.

Mamouri, R.-E. and Ansmann, A.: Potential of polarization lidar to provide profiles of CCN- and INP-relevant aerosol parameters, Atmospheric Chemistry and Physics, 16, 5905–5931, https://doi.org/10.5194/acp-16-5905-2016, https://www.atmos-chem-phys.net/16/5905/2016/, 2016.

Mariage, V., Pelon, J., Blouzon, F., Victori, S., Geyskens, N., Amarouche, N., Drezen, C., Guillot, A., Calzas, M., Garracio, M., Wegmuller, N., Sennéchael, N., and Provost, C.: IAOOS microlidar-on-buoy development and first atmospheric observations obtained during 2014 and 2015 arctic drifts, Opt. Express, 25, A73–A84, https://doi.org/10.1364/OE.25.000A73, http://www.opticsexpress.org/abstract.cfm?URI=oe-25-4-A73, 2017.

Maturilli, M.: High resolution radiosonde measurements from station Ny-Ålesund (2017-06), https://doi.org/10.1594/PANGAEA.879822, https://doi.org/10.1594/PANGAEA.879822, 2017.

McFarquhar, G. M., Ghan, S., Verlinde, J., Korolev, A., Strapp, J. W., Schmid, B., Tomlinson, J. M., Wolde, M., Brooks, S. D., Cziczo, D., Dubey, M. K., Fan, J., Flynn, C., Gultepe, I., Hubbe, J., Gilles, M. K., Laskin, A., Lawson, P., Leaitch, W. R., Liu, P., Liu, X., Lubin, D., Mazzoleni, C., Macdonald, A.-M., Moffet, R. C., Morrison, H., Ovchinnikov, M., Shupe, M. D., Turner, D. D., Xie, S., Zelenyuk, A., Bae, K., Freer, M., and Glen, A.: Indirect and Semi-direct Aerosol Campaign, Bulletin of the American Meteorological Society, 92, 183–201, https://doi.org/10.1175/2010BAMS2935.1, https://doi.org/10.1175/2010BAMS2935.1, 2011.

Mech, M., Kliesch, L.-L., Anhäuser, A., Rose, T., Kollias, P., and Crewell, S.: Microwave Radar/radiometer for Arctic Clouds (MiRAC): first insights from the ACLOUD campaign, Atmospheric Measurement Techniques, 12, 5019–5037, https://doi.org/10.5194/amt-12-5019-2019, https://www.atmos-meas-tech.net/12/5019/2019/, 2019.

Meier, W. N., Hovelsrud, G. K., van Oort, B. E. H., Key, J. R., Kovacs, K. M., Michel, C., Haas, C., Granskog, M. A., Gerland, S., Perovich, D. K., Makshtas, A., and Reist, J. D.: Arctic sea ice in transformation: A review of recent observed changes and impacts on biology and human activity, Rev. Geophys., 52, 185–217, https://doi.org/10.1002/2013rg000431, https://doi.org/10.1002/2013RG000431, 2014.

Meischner, P., Baumann, R., Höller, H., and Jank, T.: Eddy Dissipation Rates in Thunderstorms Estimated by Doppler Radar in Relation to Aircraft In Situ Measurements, Journal of Atmospheric and Oceanic Technology, 18, 1609–1627, https://doi.org/10.1175/1520-0426(2001)018<1609:EDRITE>2.0.CO;2, https://doi.org/10.1175/1520-0426(2001)018<1609:EDRITE>2.0.CO;2, 2001.

Merk, D., Deneke, H., Pospichal, B., and Seifert, P.: Investigation of the adiabatic assumption for estimating cloud micro- and macrophysical properties from satellite and ground observations, Atmospheric Chemistry and Physics, 16, 933–952, https://doi.org/10.5194/acp-16-933-2016, https://www.atmos-chem-phys.net/16/933/2016/, 2016.

Miles, N. L., Verlinde, J., and Clothiaux, E. E.: Cloud Droplet Size Distributions in Low-Level Stratiform Clouds., Journal of Atmospheric Sciences, 57, 295–311, https://doi.org/10.1175/1520-0469(2000)057<0295:CDSDIL>2.0.CO;2, 2000.

Mioche, G., Jourdan, O., Ceccaldi, M., and Delanoë, J.: Variability of mixed-phase clouds in the Arctic with a focus on the Svalbard region: a study based on spaceborne active remote sensing, Atmospheric Chemistry and Physics, 15, 2445–2461, https://doi.org/10.5194/acp-15-2445-2015, https://www.atmos-chem-phys.net/15/2445/2015/, 2015.

Mlawer, E. J., Taubman, S. J., Brown, P. D., Iacono, M. J., and Clough, S. A.: Radiative transfer for inhomogeneous atmospheres: RRTM, a validated correlated-k model for the longwave, Journal of Geophysical Research: Atmospheres, 102, 16 663–16 682, https://doi.org/10.1029/97JD00237, https://agupubs.onlinelibrary.wiley.com/doi/abs/10.1029/97JD00237, 1997.

Müller, D., Ansmann, A., Mattis, I., Tesche, M., Wandinger, U., Althausen, D., and Pisani, G.: Aerosol-type-dependent lidar ratios observed with Raman lidar, Journal of Geophysical Research: Atmospheres, 112, https://doi.org/10.1029/2006JD008292, https://agupubs.onlinelibrary.wiley.com/doi/abs/10.1029/2006JD008292, 2007.

Morrison, H., de Boer, G., Feingold, G., Harrington, J., Shupe, M. D., and Sulia, K.: Resilience of persistent Arctic mixed-phase clouds, Nature Geoscience, 5, 11–17, https://doi.org/10.1038/ngeo1332, 2012.

Morrison, H., de Boer, G., Feingold, G., Harrington, J., Shupe, M. D., and Sulia, K.: Resilience of persistent Arctic mixed-phase clouds, Nature Geoscience, 5, 11–17, https://doi.org/10.1038/ngeo1332, 2012.

Müller, D., Wandinger, U., and Ansmann, A.: Microphysical particle parameters from extinction and backscatter lidar data by inversion with regularization: theory, Appl. Opt., 38, 2346–2357, https://doi.org/10.1364/AO.38.002346, http://ao.osa.org/abstract.cfm?URI=ao-38-12-2346, 1999.

Neggers, R. e. a.: Local and remote controls on Arctic mixed-layer evolution (in submitted to JAMES), Journal of Advances in Modeling Earth Systems, 2019.

Nicholls, S.: Measurements of turbulence by an instrumented aircraft in a convective atmospheric boundary layer over the sea, Quarterly Journal of the Royal Meteorological Society, 104, 653–676, https://doi.org/10.1002/qj.49710444109, https://rmets.onlinelibrary.wiley.com/doi/abs/10.1002/qj.49710444109, 1978.

Nomokonova, T., Ebell, K., Löhnert, U., Maturilli, M., Ritter, C., and O'Connor, E.: Statistics on clouds and their relation to thermodynamic conditions at Ny-Ålesund using ground-based sensor synergy, Atmospheric Chemistry and Physics, 19, 4105–4126, https://doi.org/10.5194/acp-19-4105-2019, https://www.atmos-chem-phys.net/19/4105/2019/, 2019.

Nucciarone, J. J. and Young, G. S.: Aircraft Measurements of Turbulence Spectra in the Marine Stratocumulus-topped Boundary Layer, Journal of the Atmospheric Sciences, 48, 2382–2392, https://doi.org/10.1175/1520-0469(1991)048<2382:AMOTSI>2.0.CO;2, https://doi.org/10.1175/1520-0469(1991)048<2382:AMOTSI>2.0.CO;2, 1991.

O'Connor, E. J., Illingworth, A. J., Brooks, I. M., Westbrook, C. D., Hogan, R. J., Davies, F., and Brooks, B. J.: A Method for Estimating the Turbulent Kinetic Energy Dissipation Rate from a Vertically Pointing Doppler Lidar, and Independent Evaluation from Balloon-Borne In Situ Measurements, Journal of Atmospheric and Oceanic Technology, 27, 1652–1664, https://doi.org/10.1175/2010JTECHA1455.1, https://doi.org/10.1175/2010JTECHA1455.1, 2010.

Pithan, F. and Mauritsen, T.: Arctic amplification dominated by temperature feedbacks in contemporary climate models, Nature Geoscience, 7, 181, https://doi.org/10.1038/ngeo2071, 2014.

Porter, J. N., Miller, M., Pietras, C., and Motell, C.: Ship-Based Sun Photometer Measurements Using Microtops Sun Photometers, Journal of Atmospheric and Oceanic Technology, 18, 765–774, https://doi.org/https://doi.org/10.1175/1520-0426(2001)018<0765:SBSPMU>2.0.CO;2, https://doi.org/10.1175/1520-0426(2001)018<0765:SBSPMU>2.0.CO;2, 2001.

Radenz, M. and Seifert, P.: Software for automated trajectory analysis: trace, https://doi.org/10.5281/zenodo.2576559, https://doi.org/10.5281/zenodo.2576559, 2019.

Radenz, M., Bühl, J., Seifert, P., Griesche, H., and Engelmann, R.: peakTree: a framework for structure-preserving radar Doppler spectra analysis, Atmospheric Measurement Techniques, 12, 4813–4828, https://doi.org/10.5194/amt-12-4813-2019, https://www.atmos-meas-tech.net/12/4813/2019/, 2019.

Rose, T., Crewell, S., Löhnert, U., and Simmer, C.: A network suitable microwave radiometer for operational monitoring of the cloudy atmosphere, Atmospheric Research, 75, 183 – 200, https://doi.org/https://doi.org/10.1016/j.atmosres.2004.12.005, http://www.sciencedirect.com/science/article/pii/S0169809505000189, cLIWA-NET: Observation and Modelling of Liquid Water Clouds, 2005.

Sathe, A. and Mann, J.: A review of turbulence measurements using ground-based wind lidars, Atmospheric Measurement Techniques, 6, 3147–3167, https://doi.org/10.5194/amt-6-3147-2013, https://www.atmos-meas-tech.net/6/3147/2013/, 2013.

Schiermeier, Q.: Trapped: why 300 scientists are locking themselves in Arctic ice, Nature News Article, https://doi.org/10.1038/d41586-019-02823-x, 2019.

Schmithüsen, H.: Upper air soundings during POLARSTERN cruise PS106/1 (ARK-XXXI/1.1), https://doi.org/10.1594/PANGAEA.882736, https://doi.org/10.1594/PANGAEA.882736, 2017a.

Schmithüsen, H.: Upper air soundings during POLARSTERN cruise PS106/2 (ARK-XXXI/1.2), https://doi.org/10.1594/PANGAEA.882843, https://doi.org/10.1594/PANGAEA.882843, 2017b.

Seifert, P., Ansmann, A., Mattis, I., Wandinger, U., Tesche, M., Engelmann, R., Müller, D., Pérez, C., and Haustein, K.: Saharan dust and heterogeneous ice formation: Eleven years of cloud observations at a central European EARLINET site, J. Geophys. Res., 115, https://doi.org/10.1029/2009jd013222, https://doi.org/10.1029/2009JD013222, 2010.

Seifert, P., Kunz, C., Baars, H., Ansmann, A., Bühl, J., Senf, F., Engelmann, R., Althausen, D., and Artaxo, P.: Seasonal variability of heterogeneous ice formation in stratiform clouds over the Amazon Basin, Geophysical Research Letters, 42, 5587–5593, https://doi.org/10.1002/2015GL064068, https://agupubs.onlinelibrary.wiley.com/doi/abs/10.1002/2015GL064068, 2015.

Serreze, M. C. and Barry, R. G.: Processes and impacts of Arctic amplification: A research synthesis, Global and Planetary Change, 77, 85 – 96, https://doi.org/https://doi.org/10.1016/j.gloplacha.2011.03.004, http://www.sciencedirect.com/science/article/pii/S0921818111000397, 2011.

Shupe, M. D.: Clouds at Arctic Atmospheric Observatories. Part II: Thermodynamic Phase Characteristics, Journal of Applied Meteorology and Climatology, 50, 645–661, https://doi.org/10.1175/2010JAMC2468.1, https://doi.org/10.1175/2010JAMC2468.1, 2011.

Shupe, M. D., Kollias, P., Matrosov, S. Y., and Schneider, T. L.: Deriving Mixed-Phase Cloud Properties from Doppler Radar Spectra, Journal of Atmospheric and Oceanic Technology, 21, 660–670, https://doi.org/10.1175/1520-0426(2004)021<0660:DMCPFD>2.0.CO;2, https://doi.org/10.1175/1520-0426(2004)021<0660:DMCPFD>2.0.CO;2, 2004.

Shupe, M. D., Brooks, I. M., and Canut, G.: Evaluation of turbulent dissipation rate retrievals from Doppler Cloud Radar, Atmospheric Measurement Techniques, 5, 1375–1385, https://doi.org/10.5194/amt-5-1375-2012, https://www.atmos-meas-tech.net/5/1375/2012/, 2012.

Shupe, M. D., Persson, P. O. G., Brooks, I. M., Tjernstrom, M., Sedlar, J., Mauritsen, T., Sjogren, S., and Leck, C.: Cloud and boundary layer interactions over the Arctic sea ice in late summer, Atmospheric Chemistry and Physics, 13, 9379–9399, https://doi.org/10.5194/acp-13-9379-2013, 2013.

Siebert, H., Franke, H., Lehmann, K., Maser, R., Saw, E. W., Schell, D., Shaw, R. A., and Wendisch, M.: Probing Finescale Dynamics and Microphysics of Clouds with Helicopter-Borne Measurements, Bulletin of the American Meteorological Society, 87, 1727–1738, https://doi.org/10.1175/BAMS-87-12-1727, https://doi.org/10.1175/BAMS-87-12-1727, 2006a.

Siebert, H., Lehmann, K., and Wendisch, M.: Observations of Small-Scale Turbulence and Energy Dissipation Rates in the Cloudy Boundary Layer, Journal of the Atmospheric Sciences, 63, 1451–1466, https://doi.org/10.1175/JAS3687.1, https://doi.org/10.1175/JAS3687.1, 2006b.

SOMAG: GSM 4000 – Specifications, SOMAG AG Jena, https://www.somag-ag.de/gsm-4000/, 2017.

Sotiropoulou, G., Sedlar, J., Tjernström, M., Shupe, M. D., Brooks, I. M., and Persson, P. O. G.: The thermodynamic structure of summer Arctic stratocumulus and the dynamic coupling to the surface, Atmospheric Chemistry and Physics, 14, 12 573–12 592, https://doi.org/10.5194/acp-14-12573-2014, https://www.atmos-chem-phys.net/14/12573/2014/, 2014.

Sreenivasan, K. R.: On the universality of the Kolmogorov constant, Physics of Fluids, 7, 2778–2784, https://doi.org/10.1063/1.868656, https://doi.org/10.1063/1.868656, 1995.

Stein, A. F., Draxler, R. R., Rolph, G. D., Stunder, B. J. B., Cohen, M. D., and Ngan, F.: NOAA's HYSPLIT Atmospheric Transport and Dispersion Modeling System, Bulletin of the American Meteorological Society, 96, 2059–2077, https://doi.org/10.1175/BAMS-D-14-00110.1, https://doi.org/10.1175/BAMS-D-14-00110.1, 2015.

Stephens, G. L., Vane, D. G., Tanelli, S., Im, E., Durden, S., Rokey, M., Reinke, D., Partain, P., Mace, G. G., Austin, R., L'Ecuyer, T., Haynes, J., Lebsock, M., Suzuki, K., Waliser, D., Wu, D., Kay, J., Gettelman, A., Wang, Z., and Marchand, R.: CloudSat mission: Performance and

early science after the first year of operation, Journal of Geophysical Research: Atmospheres, 113, https://doi.org/10.1029/2008JD009982, https://agupubs.onlinelibrary.wiley.com/doi/abs/10.1029/2008JD009982, 2008.

Tjernström, M., Leck, C., Persson, P. O. G., Jensen, M. L., Oncley, S. P., and Targino, A.: The Summertime Arctic Atmosphere: Meteorological Measurements during the Arctic Ocean Experiment 2001, Bulletin of the American Meteorological Society, 85, 1305–1322, https://doi.org/10.1175/BAMS-85-9-1305, https://doi.org/10.1175/BAMS-85-9-1305, 2004.

Tjernström, M., Shupe, M. D., Brooks, I. M., Persson, P. O. G., Prytherch, J., Salisbury, D. J., Sedlar, J., Achtert, P., Brooks, B. J., Johnston, P. E., Sotiropoulou, G., and Wolfe, D.: Warm-air advection, air mass transformation and fog causes rapid ice melt, Geophys. Res. Lett., 42, 5594–5602, https://doi.org/10.1002/2015gl064373, https://doi.org/10.1002/2015GL064373, 2015.

Tjernström, M., Leck, C., Birch, C. E., Bottenheim, J. W., Brooks, B. J., Brooks, I. M., Bäcklin, L., Chang, R. Y.-W., de Leeuw, G., Di Liberto, L., de la Rosa, S., Granath, E., Graus, M., Hansel, A., Heintzenberg, J., Held, A., Hind, A., Johnston, P., Knulst, J., Martin, M., Matrai, P. A., Mauritsen, T., Müller, M., Norris, S. J., Orellana, M. V., Orsini, D. A., Paatero, J., Persson, P. O. G., Gao, Q., Rauschenberg, C., Ristovski, Z., Sedlar, J., Shupe, M. D., Sierau, B., Sirevaag, A., Sjogren, S., Stetzer, O., Swietlicki, E., Szczodrak, M., Vaattovaara, P., Wahlberg, N., Westberg, M., and Wheeler, C. R.: The Arctic Summer Cloud Ocean Study (ASCOS): overview and experimental design, Atmospheric Chemistry and Physics, 14, 2823–2869, https://doi.org/10.5194/acp-14-2823-2014, https://www.atmos-chem-phys.net/14/2823/2014/, 2014.

Uttal, T., Curry, J. A., McPhee, M. G., Perovich, D. K., Moritz, R. E., Maslanik, J. A., Guest, P. S., Stern, H. L., Moore, J. A., Turenne, R., Heiberg, A., Serreze, M. C., Wylie, D. P., Persson, O. G., Paulson, C. A., Halle, C., Morison, J. H., Wheeler, P. A., Makshtas, A., Welch, H., Shupe, M. D., Intrieri, J. M., Stamnes, K., Lindsey, R. W., Pinkel, R., Pegau, W. S., Stanton, T. P., and Grenfeld, T. C.: Surface Heat Budget of the Arctic Ocean, Bulletin of the American Meteorological Society, 83, 255–276, https://doi.org/10.1175/1520-0477(2002)083<0255:SHBOTA>2.3.CO;2, https://doi.org/10.1175/1520-0477(2002)083<0255:SHBOTA>2.3.CO;2, 2002.

Uttal, T., Starkweather, S., Drummond, J. R., Vihma, T., Makshtas, A. P., Darby, L. S., Burkhart, J. F., Cox, C. J., Schmeisser, L. N., Haiden, T., Maturilli, M., Shupe, M. D., De Boer, G., Saha, A., Grachev, A. A., Crepinsek, S. M., Bruhwiler, L., Goodison, B., McArthur, B., Walden, V. P., Dlugokencky, E. J., Persson, P. O. G., Lesins, G., Laurila, T., Ogren, J. A., Stone, R., Long, C. N., Sharma, S., Massling, A., Turner, D. D., Stanitski, D. M., Asmi, E., Aurela, M., Skov, H., Eleftheriadis, K., Virkkula, A., Platt, A., Førland, E. J., Iijima, Y., Nielsen, I. E., Bergin, M. H., Candlish, L., Zimov, N. S., Zimov, S. A., O'Neill, N. T., Fogal, P. F., Kivi, R., Konopleva-Akish, E. A., Verlinde, J., Kustov, V. Y., Vasel, B., Ivakhov, V. M., Viisanen, Y., and Intrieri, J. M.: International Arctic Systems for Observing the Atmosphere: An International Polar Year Legacy Consortium, Bulletin of the American Meteorological Society, 97, 1033–1056, https://doi.org/10.1175/BAMS-D-14-00145.1, https://doi.org/10.1175/BAMS-D-14-00145.1, 2016.

Wendisch, M., Brückner, M., Burrows, J. P., Crewell, S., Dethloff, K., Ebell, K., Lüpkes, C., Macke, A., Notholt, J., Quaas, J., Rinke, A., and Tegen, I.: Understanding causes and effects of rapid warming in the Arctic, Eos, 98, https://doi.org/10.1029/2017EO064803, 2017.

Wendisch, M., Macke, A., Ehrlich, A., Lüpkes, C., Mech, M., Chechin, D., Dethloff, K., Velasco, C. B., Bozem, H., Brückner, M., Clemen, H.-C., Crewell, S., Donth, T., Dupuy, R., Ebell, K., Egerer, U., Engelmann, R., Engler, C., Eppers, O., Gehrmann, M., Gong, X., Gottschalk, M., Gourbeyre, C., Griesche, H., Hartmann, J., Hartmann, M., Heinold, B., Herber, A., Herrmann, H., Heygster, G., Hoor, P., Jafariserajehlou, S., Jäkel, E., Järvinen, E., Jourdan, O., Kästner, U., Kecorius, S., Knudsen, E. M., Köllner, F., Kretzschmar, J., Lelli, L., Leroy, D., Maturilli, M., Mei, L., Mertes, S., Mioche, G., Neuber, R., Nicolaus, M., Nomokonova, T., Notholt, J., Palm, M., van Pinxteren, M., Quaas, J., Richter, P., Ruiz-Donoso, E., Schäfer, M., Schmieder, K., Schnaiter, M., Schneider, J., Schwarzenböck, A., Seifert, P., Shupe, M. D., Siebert, H., Spreen, G., Stapf, J., Stratmann, F., Vogl, T., Welti, A., Wex, H., Wiedensohler, A., Zanatta, M., and Zeppenfeld, S.: The Arctic Cloud Puzzle: Using ACLOUD/PASCAL Multiplatform Observations to Unravel the Role of Clouds and Aerosol Particles

in Arctic Amplification, Bulletin of the American Meteorological Society, 100, 841–871, https://doi.org/10.1175/BAMS-D-18-0072.1, https://doi.org/10.1175/BAMS-D-18-0072.1, 2019.

Wessel, P., Luis, J. F., Uieda, L., Scharroo, R., Wobbe, F., Smith, W. H. F., and Tian, D.: The Generic Mapping Tools Version 6, Geochemistry, Geophysics, Geosystems, 20, 5556–5564, https://doi.org/10.1029/2019GC008515, https://agupubs.onlinelibrary.wiley.com/doi/abs/10.1029/2019GC008515, 2019.

Winker, D. M., Pelon, J. R., and McCormick, M. P.: CALIPSO mission: spaceborne lidar for observation of aerosols and clouds, https://doi.org/10.1117/12.466539, https://doi.org/10.1117/12.466539, 2003.

Winker, D. M., Pelon, J., Coakley, J. A., Ackerman, S. A., Charlson, R. J., Colarco, P. R., Flamant, P., Fu, Q., Hoff, R. M., Kittaka, C., Kubar, T. L., Le Treut, H., Mccormick, M. P., Mégie, G., Poole, L., Powell, K., Trepte, C., Vaughan, M. A., and Wielicki, B. A.: The CALIPSO Mission, Bulletin of the American Meteorological Society, 91, 1211–1230, https://doi.org/10.1175/2010BAMS3009.1, https://doi.org/10.1175/2010BAMS3009.1, 2010.

Wulfmeyer, V. and Janjić, T.: Twenty-Four-Hour Observations of the Marine Boundary Layer Using Shipborne NOAA High-Resolution Doppler Lidar, Journal of Applied Meteorology, 44, 1723–1744, https://doi.org/10.1175/JAM2296.1, https://doi.org/10.1175/JAM2296.1, 2005.

Yeo, H., Park, S.-J., Kim, B.-M., Shiobara, M., Kim, S.-W., Kwon, H., Kim, J.-H., Jeong, J.-H., Park, S. S., and Choi, T.: The observed relationship of cloud to surface longwave radiation and air temperature at Ny-Ålesund, Svalbard, Tellus B: Chemical and Physical Meteorology, 70, 1–10, https://doi.org/10.1080/16000889.2018.1450589, https://doi.org/10.1080/16000889.2018.1450589, 2018.

Yin, Z., Ansmann, A., Baars, H., Seifert, P., Engelmann, R., Radenz, M., Jimenez, C., Herzog, A., Ohneiser, K., Hanbuch, K., Blarel, L., Goloub, P., Dubois, G., Victori, S., and Maupin, F.: Aerosol measurements with a shipborne Sun–sky–lunar photometer and collocated multiwavelength Raman polarization lidar over the Atlantic Ocean, Atmospheric Measurement Techniques, 12, 5685–5698, https://doi.org/10.5194/amt-12-5685-2019, https://www.atmos-meas-tech.net/12/5685/2019/, 2019.

Young, G., Jones, H. M., Choularton, T. W., Crosier, J., Bower, K. N., Gallagher, M. W., Davies, R. S., Renfrew, I. A., Elvidge, A. D., Darbyshire, E., Marenco, F., Brown, P. R. A., Ricketts, H. M. A., Connolly, P. J., Lloyd, G., Williams, P. I., Allan, J. D., Taylor, J. W., Liu, D., and Flynn, M. J.: Observed microphysical changes in Arctic mixed-phase clouds when transitioning from sea ice to open ocean, Atmospheric Chemistry and Physics, 16, 13 945–13 967, https://doi.org/10.5194/acp-16-13945-2016, https://www.atmos-chem-phys.net/16/13945/2016/, 2016.

Zhang, D., Wang, Z., Heymsfield, A., Fan, J., and Luo, T.: Ice Concentration Retrieval in Stratiform Mixed-Phase Clouds Using Cloud Radar Reflectivity Measurements and 1D Ice Growth Model Simulations, Journal of the Atmospheric Sciences, 71, 3613–3635, https://doi.org/10.1175/JAS-D-13-0354.1, https://doi.org/10.1175/JAS-D-13-0354.1, 2014.

Zhou, M. Y., Lenschow, D. H., Stankov, B. B., Kaimal, J. C., and Gaynor, J. E.: Wave and Turbulence Structure in a Shallow Baroclinic Convective Boundary Layer and Overlying Inversion, Journal of the Atmospheric Sciences, 42, 47–57, https://doi.org/10.1175/1520-0469(1985)042<0047:WATSIA>2.0.CO;2, https://doi.org/10.1175/1520-0469(1985)042<0047:WATSIA>2.0.CO;2, 1985.